

Lift reversal for an oblate droplet translating in a linear shear flow: from inviscid bubble to rigid spheroid

Jie Zhang¹ , Bo-Lin Wei¹, Wei-Jing Meng¹ and Ming-Jiu Ni² 

¹State Key Laboratory for Strength and Vibration of Mechanical Structures, School of Aerospace, Xi'an Jiaotong University, Xi'an, Shaanxi 710049, PR China

²School of Engineering Science, University of Chinese Academy of Sciences, Beijing 101408, PR China

Corresponding author: Jie Zhang, j_zhang@xjtu.edu.cn

(Received 11 August 2024; revised 16 January 2025; accepted 24 January 2025)

When an oblate droplet translates through a viscous fluid under linear shear, it experiences a lateral lift force whose direction and magnitude are influenced by the Reynolds number, the droplet's viscosity and its aspect ratio. Using a recently developed sharp interface method, we perform three-dimensional direct numerical simulations to explore the evolution of lift forces on oblate droplets across a broad range of these parameters. Our findings reveal that in the low-but-finite Reynolds number regime, the Saffman mechanism consistently governs the lift force. The lift increases with the droplet's viscosity, aligning with the analytical solution derived by Legendre & Magnaudet (*Phys. Fluids*, vol. 9, 1997, p. 3572), and also rises with the droplet's aspect ratio. We propose a semi-analytical correlation to predict this lift force. In the moderate- to high-Reynolds-number regime, distinct behaviours emerge: the L - and S -mechanisms, arising from the vorticity contained in the upstream shear flow and the vorticity produced at the droplet surface, dominate for weakly and highly viscous droplets, respectively. Both mechanisms generate counter-rotating streamwise vortices of opposite signs, leading to observed lift reversals with increasing droplet viscosity. Detailed force decomposition based on vorticity moments indicates that in the L -mechanism-dominated regime for weakly to moderately viscous droplets, the streamwise vorticity-induced lift approximates the total lift. Conversely, in the S -mechanism-dominated regime, for moderately to highly viscous droplets, the streamwise vorticity-induced lift constitutes only a portion of the total lift, with the asymmetric advection of azimuthal vorticity at the droplet interface contributing additional positive lift to counterbalance the S -mechanism's effects. These

insights bridge the understanding between inviscid bubbles and rigid particles, enhancing our comprehension of the lift force experienced by droplets in different flow regimes.

Key words: bubble dynamics, drops, multiphase flow

1. Introduction

Droplet distributions and their effects on flow structures play a critical role in numerous geophysical and industrial processes. In such scenarios involving droplet flows, a pivotal factor influencing the evolution of these distributions is the lateral, or lift, force acting on droplets as they rise in shear flows. Recent advances in experimental techniques and numerical methods have significantly enhanced our understanding of the lift force experienced by inviscid bubbles and rigid spheres in shear flows. These entities represent the two extremes of viscous droplets, corresponding to zero and infinite viscosity compared with the external fluid.

For an inviscid bubble rising in shear flow, it is well established that a clean, spherical bubble experiences a positive lift force (Legendre & Magnaudet 1998; Kurose *et al.* 2001), causing it to preferentially migrate towards the region with higher velocity past it. However, the mechanisms responsible for lift generation differ between the low-but-finite and moderate- to high-Reynolds-number regimes. In the low-Reynolds-number regime, the Saffman mechanism is dominant, arising from the asymmetric convection of azimuthal vorticities produced at the bubble's interface in the presence of shear (Saffman 1965; Ervin & Tryggvason 1997). In contrast, the *L*-mechanism, based on Lighthill's seminal work (Lighthill 1956; Legendre & Magnaudet 1998), involves the tilting of vorticity contained within the shear flow by the presence of the bubble, generating streamwise vorticities that produce a positive lift force in the moderate- to high-Reynolds-number regime. Recent numerical studies by Adoua *et al.* (2009) have shown that the migration direction of bubbles in shear flow can reverse when their size and deformation exceed a critical value. Similar findings regarding bubble shape have been reported in experiments, notably by Tomiyama and collaborators (Tomiyama *et al.* 2002; Aoyama *et al.* 2017; Hayashi *et al.* 2020, 2021). This intriguing reversal phenomenon contradicts predictions from inviscid theory, as Naciri (1992) derived that the lift of an oblate bubble should have the same sign as that of a spherical bubble. Adoua *et al.* (2009) identified the *S*-mechanism, responsible for lift reversal in highly deformed bubbles, where the stretching and tilting of vorticity produced at the bubble surface are transformed into streamwise vorticities, resulting in negative lift forces. Despite these findings, qualitative comparisons between numerical results and experimental observations reveal significant discrepancies. In experiments, lift reversal occurs at relatively smaller aspect ratios and lower Reynolds numbers compared with simulations. Two possible explanations have been proposed for these discrepancies. First, the presence of surfactants in experiments may prevent the shear-free condition at the gas–liquid interface from being fully satisfied, enhancing the *S*-mechanism by generating more vorticity at the bubble surface. Second, the bubble shapes observed in experiments often deviate from oblate spheroids and become fore-aft asymmetric. More particularly, they can even exhibit left-right asymmetry (Taylor 1932; Ervin & Tryggvason 1997; Tomiyama *et al.* 2002; Magnaudet *et al.* 2003), a phenomenon termed the *A*-mechanism (Zhang *et al.* 2021; Hidman *et al.* 2022).

The other extremity corresponds to a rigid particle moving in linear shear flow, representing a droplet with infinite viscosity compared with the external fluid. For a non-rotating solid sphere, the Saffman mechanism remains dominant at small but non-zero

Reynolds numbers. Saffman (Saffman 1965) provided an analytical solution for the lift force on a rigid sphere in this regime, valid when the inertial effects associated with translational slip motion become comparable to viscous effects. Subsequent efforts by various researchers (Asmolov 1990; McLaughlin 1991; Mei 1992; Legendre & Magnaudet 1998) extended Saffman's solution to more general conditions within the low-but-finite Reynolds number regime. However, these solutions were often either semi-empirical, relying on specific numerical data or semi-analytical, neglecting lift contributions from the sub-Oseen region. Thus, the applicability of these lift correlations in this regime requires further investigation. In contrast, at moderate to high Reynolds numbers, the lift coefficient of a solid sphere does not maintain positive values like that of an inviscid spherical bubble. Instead, it decreases with increasing Reynolds number, eventually becoming negative and strongly dependent on the shear rate beyond a certain threshold. This trend has been consistently observed in direct numerical simulations (Kurose & Komori 1999; Bagchi & Balachandar 2002; Sugioka & Komori 2007; Hölzer & Sommerfeld 2009), although the specific Reynolds number at which lift reversal occurs varies among studies due to differences in numerical settings, particularly in terms of the size of the computational domain (Shi & Rzehak 2019). This lift reversal phenomenon occurs because the attached eddies behind the sphere, present at high Reynolds numbers, become tilted in the presence of ambient shear. This tilting generates counter-rotating streamwise vortices that produce negative lift forces. This mechanism is analogous to the *S*-mechanism observed on oblate bubbles, where the symmetry break of azimuthal vorticities results in negative lift forces on a rigid sphere. However, as far as the authors are aware, no studies have been conducted on the lift force experienced by an ellipsoidal spheroid, while most studies concern the torques.

Shi and collaborators recently reviewed the behaviour of inviscid spherical bubbles and rigid spheres translating in linear shear flow (Shi & Rzehak 2019; Shi *et al.* 2020, 2021). Building on this state-of-the-art research, it is clear that the migration direction of a body translating in shear flow depends significantly on several factors: the Reynolds number based on translational slip velocity (i.e. low-but-finite or moderate to high values), the interfacial condition of the body (i.e. free slip or no-slip) and the body's oblateness (i.e. sphere or ellipsoid). However, there remains a gap in understanding how to bridge the behaviours of inviscid bubbles and rigid spheroids translating in shear flow. Specifically, droplets can contain fluids with arbitrary viscosities ranging from zero to infinity compared with the external fluid. This study aims to address the following questions through three-dimensional (3-D) direct numerical simulations.

- (i) Low-but-finite Reynolds number regime. The Saffman mechanism typically dominates regardless of the interfacial condition. How does the Saffman mechanism evolve as the viscosity of the droplet varies from zero to infinity compared with the external fluid?
- (ii) Moderate- to high-Reynolds-number regime. The lateral lift force acting on an inviscid bubble is always positive, while it may become negative for a rigid sphere. How does this lift reversal depend on the droplet's viscosity? Furthermore, what is the relationship between lift reversal and the sign reversal of the streamwise vorticities?
- (iii) Oblateness of the droplet. In both the low-but-finite and moderate- to high-Reynolds-number regimes, what role does the oblateness of the droplet play in generating a lift force?

For the first problem, Legendre & Magnaudet (1997) extended Saffman's (Saffman 1965) and McLaughlin's (McLaughlin 1991) analyses to a spherical droplet of arbitrary

viscosity. They found that the lift force on a spherical bubble is $(2/3)^2$ times that of a solid sphere, where the coefficient $2/3$ corresponds to the ratio of the magnitude of the vorticity at the surface of each body type. However, this analytical solution has not yet been verified for droplets with arbitrary viscosity and our numerical work aims to confirm its validity. For the second problem, the influence of surfactants on the lift force of a bubble rising in shear flow presents a similar issue. Previous studies using numerical simulations (Fukuta *et al.* 2008) and experiments (Hayashi & Tomiyama 2018; Chen *et al.* 2023) have shown that surfactant contamination can cause the lift on a bubble to reverse to a small negative value, making it behave more like a rigid sphere. However, the details of how a real droplet migrates in linear shear flow remain unclear, and results from studies involving surfactants shed some light for our research. For the final problem, Adoua *et al.* (2009) and Hidman *et al.* (2022) demonstrated that the L - and S -mechanisms compete when the oblateness of an inviscid bubble is varied. It is still of great interest to determine the role of ellipticity in the shape of a droplet with arbitrary viscosity.

To address these three problems, we developed an accurate and rigorous numerical method capable of simulating shear flow past a frozen droplet with arbitrary shape and viscosity. This method uses a Cartesian grid technique combined with the embedded boundary method, allowing for the fluid flow to be solved in separate liquid domains both interior and exterior to the droplet interface. Additionally, this approach imposes the jump conditions across the interface more flexibly than traditional body-fitted grids, as the grids are automatically generated to accommodate droplets with varying aspect ratios. It is important to note that there are also interface tracking methods (e.g. the volume of fluid, level set and front tracking) for studying such problems (Ervin & Tryggvason 1997; Zhang *et al.* 2021; Hidman *et al.* 2022). These methods allow the bubble or droplet to rise and deform freely under the influence of buoyancy, providing detailed information on the kinematics of body motion, rotation and possible shape variations, as well as the structure of the flow field. However, they do not provide insight into the mechanisms that disentangle the individual factors contributing to the observed motion. The ‘frozen-body’ system we employ enables us to isolate the mechanisms caused by different influential factors, such as the viscosity and deformation of the droplet.

The manuscript is structured as follows. In § 2, we describe the physical configuration and mathematical formulation. The numerical methodology and validation tests are introduced in § 3. Sections 4 and 5 present the numerical results corresponding to low-but-finite and moderate- to high-Reynolds-number regimes, respectively, highlighting the evolution of the lift force experienced by the droplet under varying parameters and, particularly, the aspect ratio of the droplet is investigated. These findings provide valuable insights into the production of lift force under different conditions, with in-depth mechanisms discussed in § 6. Finally, the conclusions are succinctly summarised in § 7, culminating in a comprehensive synthesis of our research contributions.

2. Statement of the problem

The present study aims to investigate the lift forces experienced by a viscous droplet translating in an unbounded linear shear flow, where the droplet is assumed to neither deform, rotate nor drift in the transverse direction. Figure 1 illustrates this problem, noting that the reference frame moves with the droplet, allowing the droplet to remain stationary in the numerical simulations while the shear flow passes it and generates the associated internal flow. The Cartesian coordinate system is also depicted in the figure, with the incoming flow expressed as $\mathbf{U}(y) = (U_\infty + \alpha y)\mathbf{e}_x$. This indicates that the ambient flow is along the x -direction and has a shear rate α parallel to the y -axis, resulting in a

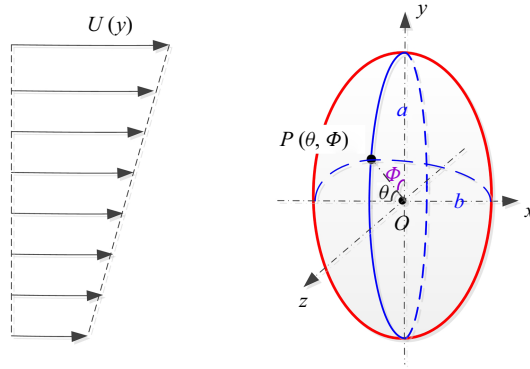


Figure 1. Diagram illustrating the configuration of a linear shear flow past a viscous droplet.

non-zero spanwise vorticity of $\boldsymbol{\omega}_\infty = -\alpha \mathbf{e}_z$ within the ambient flow. Additionally, polar coordinates are sometimes used to describe the problem, with the meridian direction θ and the azimuthal direction ϕ defined, as shown at the local interfacial point P in the illustration. Furthermore, figure 1 considers the droplet with a prescribed oblate shape described by the equation $x^2/b^2 + y^2/a^2 + z^2/a^2 = 1$, with $a \geq b$. This configuration is chosen so that the principal plane YOZ always faces the incoming flow.

For a rising bubble, the internal gas flow is negligible due to its much lower viscosity compared with the external liquid, resulting in almost zero tangential stress at the bubble interface and yielding a free slip boundary condition. Conversely, a rigid particle, with its internal viscosity considered infinite compared with the external fluid, has a no-slip boundary condition prescribed at the interface. However, simulating a viscous liquid droplet translating in an ambient liquid requires computing both the internal and external flows. This leads to the following incompressible mass and momentum equations:

$$\nabla \cdot \mathbf{u}_k = 0, \quad \rho_k \left(\frac{\partial \mathbf{u}_k}{\partial t} + \mathbf{u}_k \cdot \nabla \mathbf{u}_k \right) = -\nabla p_k + \nabla \cdot 2\mu_k \mathbb{S}_k, \quad (2.1)$$

where ρ_k , μ_k , \mathbf{u}_k and p_k are the density, viscosity, velocity and pressure of the corresponding fluid, with $k = i$ and e denoting the internal and external fluids, respectively. In addition, $\mathbb{S}_k = [\nabla \mathbf{u}_k + \nabla \mathbf{u}_k^T]/2$ is the rate of the strain tensor.

The closed-form solution of the velocity and pressure in (2.1) requires pre-known interfacial conditions of the droplet, consisting of the no penetration condition, the continuity of tangential velocities and the continuity of tangential stresses, which are respectively expressed as follows:

$$\left. \begin{aligned} \mathbf{u}_e \cdot \mathbf{n} &= \mathbf{u}_i \cdot \mathbf{n} = 0 \\ \mathbf{n} \times \mathbf{u}_e &= \mathbf{n} \times \mathbf{u}_i \\ \mathbf{n} \times (\mu_e \mathbb{S}_e \cdot \mathbf{n}) &= \mathbf{n} \times (\mu_i \mathbb{S}_i \cdot \mathbf{n}) \end{aligned} \right\} \text{ at } \Gamma, \quad (2.2)$$

where Γ is the droplet interface and \mathbf{n} denotes the local normal vector of the interface directed towards the external fluid. The tangential components of the velocity and stresses are along two principal directions of curvature, denoted as \mathbf{t}_1 and \mathbf{t}_2 at the local point P . As will be discussed later in § 3 and Appendix A, implementing such partial slip boundary conditions presents significant challenges in developing numerical methods within the Cartesian system, as Γ does not necessarily coincide with the grid boundaries. In particular, determining the local \mathbf{t}_1 and \mathbf{t}_2 in numerical simulations introduces additional complexities when dealing with an arbitrarily shaped droplet.

Several dimensionless parameters can be used to characterise the problem: the Reynolds number Re , the dimensionless shear rate Sr , the viscosity ratio μ^* , the density ratio ρ^* and the aspect ratio of the droplet χ . These are defined as follows:

$$Re_k = \frac{2\rho_k U_\infty R}{\mu_k}, \quad Sr = \frac{2\alpha R}{U_\infty}, \quad \mu^* = \frac{\mu_i}{\mu_e}, \quad \rho^* = \frac{\rho_i}{\rho_e}, \quad \chi = \frac{a}{b}, \quad (2.3)$$

where the volume-equivalent radius $R = (ab^2)^{1/3}$ is employed as the characteristic length in this study. Note that some other works (Adoua *et al.* 2009; Blanco & Magnaudet 1995) use the major axis a of the spheroid to characterise the length, so the problems are not the same even if our dimensionless parameters appear identical to those in their studies. Selecting $2R$ to define Re and Sr , while maintaining the volume of the spheroid as a constant, facilitates the investigation of the influence of χ on the flow behaviours. Additionally, there are two Reynolds numbers characterising the internal and external flows of the droplet, Re_i and Re_e . Keep in mind that they are not independent but related by $Re_i = Re_e \rho_i \mu_e / \rho_e \mu_i$. Consequently, there are actually five dimensionless parameters governing this problem: the external Reynolds number Re_e , the Reynolds number ratio $Re^* = Re_i / Re_e$, the viscosity ratio μ^* , the shear rate Sr and the aspect ratio χ . However, it is not feasible to explore the influences of all these dimensionless parameters in a single paper. Therefore, we mainly focus on three of them: Re_e , which weights the inertial effect of the ambient flow; μ^* , which bridges the gap between the inviscid bubble and the rigid particle; and χ , which describes the oblateness of the droplet. The impacts of the other two parameters, Sr and Re^* , will be discussed briefly in § 6 and Appendix E, respectively.

In addition, we are particularly interested in obtaining the lift forces acting on the droplet as these dimensionless parameters vary. Since the shear is maintained in the \mathbf{e}_y direction, the lift force produced by the shear is always parallel to \mathbf{e}_y . This leads us to define the lift force as follows:

$$F_L = \mathbf{e}_y \cdot \int_{\Gamma} (-p\mathbb{I} + 2\mu\mathbb{S}) \cdot \mathbf{n} \, d\Gamma. \quad (2.4)$$

We also provide the dimensionless counterpart of the lift force by dividing by the corresponding force dimension, $\pi R^2 \rho_e U_\infty^2 / 2$, yielding the lift coefficient C_L . Note that a positive C_L indicates that the lift force pushes the droplet towards the side with higher incoming velocity (positive y) and *vice versa*. Furthermore, (2.4) implies that the force coefficients can be split into the pressure (C_p) and viscous (C_μ) components. It is important to note that in some studies (Legendre & Magnaudet 1998; Adoua *et al.* 2009), the lift coefficient is calculated as $C_{L,\alpha} = F_L / (\frac{4}{3}\pi R^3 \rho_e U_\infty \alpha)$ and, thus, these two shear-lift coefficients are related by $C_{L,\alpha} = 3C_L / 4Sr$. Throughout the present study, we will use C_L as the standard lift coefficient.

In addition, it is important to note that a droplet translating in shear flow also experiences a drag force parallel to \mathbf{e}_x (i.e. by replacing \mathbf{e}_y with \mathbf{e}_x in (2.4)) and hydrodynamic torques. However, in this manuscript, we do not intend to present every aspect of the problem, but focus solely on the evolution of the lift force, thus the drag- and the torque-induced rotation are not considered. Appendix A demonstrates that the drag forces obtained in this study are in good agreement with available references, and the observation that the shear rate has little impact on drag compared with that in homogeneous flow is consistent with many other studies (Legendre & Magnaudet 1998; Bagchi & Balachandar 2002; Adoua *et al.* 2009).

3. Numerical methods and numerical settings

3.1. Numerical methods

The computations presented in this study were performed using our recently developed numerical method, which was initially described and validated in our previous work on the flow past bubbles (Fang *et al.* 2021). Previously, this numerical tool was limited to handling oblate inviscid bubbles ($\mu^* = 0$) and rigid spheroids ($\mu^* = \infty$). However, recent advancements in the numerical method, as thoroughly described by Wei *et al.* (2023), have extended its applicability to droplets with irregular shapes and arbitrary viscosities. In this section, together with Appendix A, we will briefly introduce the key features of the method, while more comprehensive details can be found in a separate publication (Wei *et al.* 2023).

As described in § 2, the main challenge in solving (2.1) is to accurately impose the interfacial boundary conditions (2.2) at the droplet interface. The boundary conditions (2.2) can be reformulated as follows:

$$\left. \begin{aligned} u_{e,n} &= u_{i,n} = 0 \\ \mu_e \left(\frac{\partial u_{e,\tau_1}}{\partial n} - \kappa_1 u_{e,\tau_1} \right) &= \mu_i \left(\frac{\partial u_{i,\tau_1}}{\partial n} - \kappa_1 u_{i,\tau_1} \right) \\ \mu_e \left(\frac{\partial u_{e,\tau_2}}{\partial n} - \kappa_2 u_{e,\tau_2} \right) &= \mu_i \left(\frac{\partial u_{i,\tau_2}}{\partial n} - \kappa_2 u_{i,\tau_2} \right) \end{aligned} \right\} \text{ at } \Gamma, \quad (3.1)$$

with n , τ_1 and τ_2 denoting the normal component and the two principal tangential components along \mathbf{n} , \mathbf{t}_1 and \mathbf{t}_2 , respectively, while κ_1 and κ_2 are the corresponding interface curvatures in these two directions. This set of equations represents the kinematic jump conditions across the droplet interface. Specifically, when $\mu_i = 0$, these conditions simplify to the free-slip boundary condition and when $\mu_i = \infty$, they simplify to the no-slip boundary condition.

Moreover, such kinematic jumps can be easily imposed on body-fitted grids, where the grid boundaries perfectly coincide with the droplet interface. However, while body-fitted grids can accurately impose these jump conditions on a spherical droplet, they are less effective for oblate droplets (Legendre *et al.* 2019; Rachih *et al.* 2020). To address this challenge, we have developed a novel numerical methodology within the framework of Cartesian grids (Wei *et al.* 2023). This approach is non-trivial because the grid boundaries do not align with the droplet interface, leading to the partitioning of interfacial grids into interior and exterior regions of the droplet. Accurately imposing jump conditions on such meshes is particularly challenging when the droplet has an irregular shape. This task heavily relies on the precise estimation of local principal curvatures within the interfacial cells, denoted as κ_1 and κ_2 . The numerical method proposed in our recent work incorporates two key techniques to address this issue. First, a height function method is employed to determine the principal curvatures and their directions in the interfacial cells. Second, the internal and external flows (2.1) are solved simultaneously using an embedded boundary method, which ensures the correct implementation of the jump conditions described in (3.1). Detailed descriptions of these techniques can be found from Wei *et al.* (2023) and additional information about the numerical algorithms is provided in Appendix A. For simplicity, we will not elaborate further here.

We implemented this numerical method using the open-source library *Basilisk* (Popinet 2003, 2015), which employs the finite volume method to discretise the equations, thereby preserving their conservative properties. In general, *Basilisk* uses an approximate projection method to decouple the velocity and pressure equations (2.1). The well-known Bell–Colella–Glaz scheme (Bell *et al.* 1989) is employed for discretising the convection

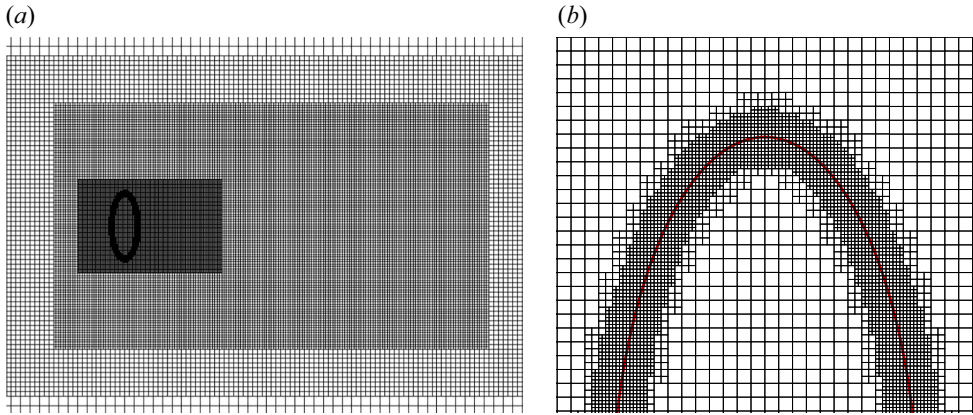


Figure 2. Grid distribution within the computational domain for the parameters $(Re_e, Re^*, \mu^*, \chi) = (200, 1.0, 100, 2.0)$. (a) Global view of the computational grid. (b) Enlarged view near the droplet surface. The grid resolution reaches a minimum size of $\Delta = R/80$ in the vicinity of the droplet, with 10 layers extending both inside and outside of the interface.

term, while a fully implicit scheme is used for the viscous term. Additionally, *Basilisk* incorporates an adaptive mesh refinement technique to enhance computational efficiency by refining the mesh in regions close to the interface and those with concentrated vorticity. Detailed descriptions of these algorithms can be found in the references by Popinet (2003, 2015) and we do not reiterate them here. It is worth noting that the original *Basilisk* library was designed to simulate flow past rigid particles with no-slip boundary conditions. Extending these algorithms to handle droplets with arbitrary viscosity constitutes our novel contribution in developing the numerical method.

Appendix A includes validation tests, specifically focusing on benchmark problems involving shear flow past a frozen body. These tests have been conducted to verify the accuracy and validity of the aforementioned numerical methods for simulating three-dimensional flows past a viscous droplet.

3.2. Numerical settings

The simulations were conducted in a three-dimensional cubic domain with dimensions $L \times L \times L$. The droplet is positioned at the origin $(x, y, z) = (0, 0, 0)$. The inlet (left boundary) is located $L/3$ to the left of the droplet, while the outlet (right boundary) is situated $2L/3$ to the right. The droplet is centred along the other four walls of the domain. Figure 2 illustrates the non-uniform mesh employed in the simulations for the case with $Re_e = Re_i = 200$, $\mu^* = 100$, $\chi = 2.0$ and $Sr = 0.2$. Figure 2(a) provides a global view of the mesh system, while figure 2(b) shows a close-up view near the droplet. The mesh features a smallest grid size of $\Delta = R/80$ near the droplet interface, with 10 layers of grids both interior and exterior to the interface. This configuration allows for accurate resolution of the flow boundary layer, which has a thickness $\delta \propto 2R/\sqrt{Re} \simeq R/7$. Consequently, there are at least 11 grid points within the boundary layer. Further, grids with a slightly larger size of $\Delta = R/20$ extend to the upstream and downstream regions of the droplet, covering distances of $2R$ and $5R$, respectively. Grids with a size of $\Delta = R/10$ then expand to a broader range of $[-5R, 15R]$. This strategy of spatial resolution ensures precise capture of the shear flow around the droplet and accurate depiction of the wake region. Additional numerical tests for grid independence, detailed in Appendix A, confirm that this spatial resolution is sufficient for converging results on the forces experienced by the droplet.

Another important consideration is determining the optimal size for the computational domain. This is crucial when investigating flows around a blunt body, particularly at low Reynolds numbers, where confinement effects from a smaller computational domain can significantly influence the results (Legendre & Magnaudet 1998). To address this, a size-independent study was conducted for two different Reynolds numbers on a bubble: $Re_e = 0.1$ and $Re_e = 200$, representing low- and moderately high- Re regimes, respectively. The domain size was varied from $L = 50R$ to $L = 800R$ and results from different domain sizes are detailed in Appendix A. It is evident that a domain size of $L = 400R$ provides convergence for the low-Reynolds-number case, while $L = 100R$ already achieves convergence for the high-Reynolds-number case. Consequently, $L = 400R$ and $200R$ were selected for the simulations in these two Re regimes reported in the manuscript. Note that simulations were not performed at Reynolds numbers lower than 0.1 due to the excessive domain size requirements. Furthermore, the case with $Re_e = 0.1$ sufficiently captures the asymptotic behaviour for the low-Reynolds-number limit.

In addition to the interfacial boundary conditions at the droplet, appropriate boundary conditions must be specified for the computational domain. A straightforward approach would be to set an inflow velocity $\mathbf{U} = (U_\infty + \alpha y)\mathbf{e}_x$ at the left boundary ($x = -L/3$) and a parabolic outflow condition at the right boundary ($x = 2L/3$). However, these settings can lead to numerical instability for this shear flow problem. Specifically, the unperturbed velocity $U_x = \mathbf{U} \cdot \mathbf{e}_x$ becomes negative in the region where $y < -U_\infty/\alpha$, resulting in a reversal of the inlet and outlet boundaries in this negative U_x region. Consequently, the unique inflow (outflow) condition at the left (right) boundary becomes non-physical, potentially leading to numerical disturbances that compromise the accuracy of the simulations. To address this issue, Legendre & Magnaudet (1998) proposed a hybrid boundary condition at the downstream boundary. This method involves imposing the standard outflow condition for the region within the disk $(y^2 + z^2)^{1/2} < U_\infty/\alpha$, while applying the inflow condition $(U_\infty + \alpha y)$ for the region outside this disk $(y^2 + z^2)^{1/2} > U_\infty/\alpha$. In our study, we tested several boundary condition configurations to minimise numerical contamination in the flow field. Ultimately, we found that applying periodic boundary conditions at both the upstream and downstream boundaries yielded the most reliable results. Validation tests presented in Appendix A also support the effectiveness of this approach. Additionally, no-slip conditions, $\mathbf{U} = (U_\infty + \alpha y)\mathbf{e}_x$, are applied to the four lateral walls (top, bottom, front and back) of the domain.

As previously noted, the problem under investigation is characterised by five dimensionless parameters ($Re_e, Sr, Re^*, \mu^*, \chi$). However, our focus is not on creating a comprehensive phase map of flow features based on these parameters. Instead, we concentrate primarily on the phenomenon of lift reversal as the droplet transitions from an inviscid oblate bubble to a rigid spheroid. Therefore, in §§ 4 and 5, we focus on the shear rate of $Sr = 0.2$, while the effects of varying the shear rate are discussed in § 6. Throughout this study, we investigate only one Reynolds number ratio, $Re^* = 1$. Although exploring additional values of Re^* could be insightful, given that some studies (Edelmann *et al.* 2017; Rachih 2019; Shi *et al.* 2024) have identified secondary flow instabilities at higher Re^* values, a detailed examination of Re^* is beyond the scope of the current work. A brief discussion of such secondary instabilities is provided in Appendix E, while a more comprehensive discussion of this scenario can be found in the very recent work by Shi *et al.* (2024), almost in synchronisation with the present study. For simplicity, we will use Re throughout the manuscript, as Re_e and Re_i are equivalent in this study. In summary, our primary focus is on the lift response of the droplet by varying Re, μ^* and χ , within the ranges $Re \in [0.1, 300]$, $\mu^* \in [0.01, 100]$ and $\chi \in [1.0, 2.5]$. Particularly, cases

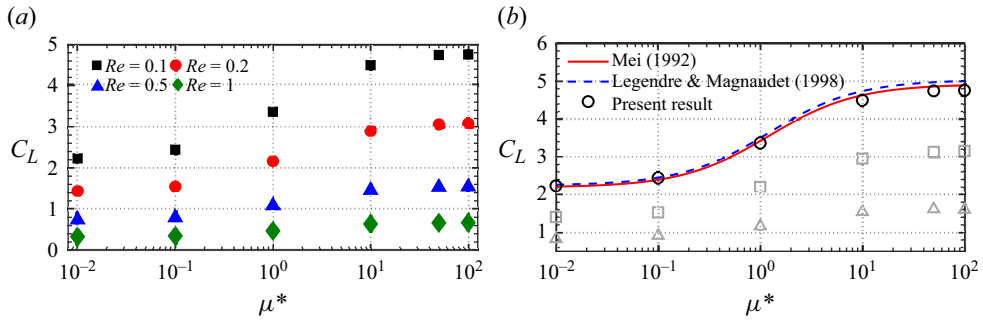


Figure 3. Lift coefficients C_L experienced by spherical droplets in the low-but-finite Re regime, with variations in the Reynolds number and viscosity ratio. (a) C_L as a function of μ^* at different Re . (b) Comparison between numerical results and analytical correlations for spherical droplets at $Re = 0.1$; the solid line represents (4.1), (4.2a) from Mei (1992), and the dashed line is (4.1), (4.2b) from Legendre & Magnaudet (1998), while for both lines, we use $C(\mathcal{R}) \propto \mathcal{R}^2$ in (4.1) predicted by Legendre & Magnaudet (1997). The grey triangles and squares in panel (b) indicate the pressure and viscous components of the lift coefficients, respectively.

with $\mu^* = 0.01$ and $\mu^* = 100$ are used to model an inviscid bubble and a rigid spheroid, respectively, in the numerical simulations.

4. Low-but-finite Re regime

In this section, we focus on investigating the lift forces experienced by the droplet within the range of low-but-finite Reynolds numbers ($0.1 \leq Re \leq 1$). Specifically, we explore how the lift changes as the droplet transitions from an inviscid oblate bubble to a rigid spheroid, corresponding to the parameter ranges $(\mu^*, \chi) = (0.01, 1.0-2.5)$ and $(\mu^*, \chi) = (100, 1.0-2.5)$, respectively.

4.1. Spherical droplets

To begin with, we focus on spherical droplets. Figure 3(a) presents the lift forces experienced by these droplets, which have varying Reynolds numbers and viscosity ratios but a constant shear rate of $Sr = 0.2$. The results show that the lift coefficient $C_L(Re, \mu^*, \chi = 1.0)$ increases with μ^* but decreases with Re . To understand this trend, it is important to review the state-of-the-art of this problem in the low-but-finite Reynolds number regime. It was Saffman (1965) who first used the asymptotic method to investigate the lift force acting on a particle in the low-Reynolds-number regime with a very high shear rate, under the assumption that the flow in the far field is equivalent to that produced by a point force (whose magnitude is the Stokes drag on the particle) located at the particle's position. This point force, combined with advective effects induced by the ambient shear, results in a small correction to the far-field flow, which takes the form of a uniform flow at leading order. This uniform flow is not aligned with the upstream flow, due to the asymmetry introduced by the shear. The force resulting from this small correction is a small Stokes drag, whose direction is collinear to the flow correction, i.e. it is not collinear to the upstream flow. The force component perpendicular to the upstream flow is the Saffman lift force, also known as the Saffman mechanism. In addition, the origin of the primary Stokes drag is the azimuthal vorticity at the particle surface: in the Stokes limit, the force and the vorticity share the same pre-factor. Hence, increasing the magnitude of the vorticity, by changing the particle shape or the boundary condition, results in an increase of the drag and *vice versa*. Advection in the wake is key to obtaining a non-zero

lift force, as reversibility in the Stokes limit prevents the existence of a lift component for a sphere (Bretherton 1962). For the wake to produce a lift force, some asymmetry is required; otherwise, the wake only provides the Oseen drag correction. Clearly, shear is responsible for this asymmetry and, thus, the Saffman mechanism can also be understood as stemming from the asymmetric convection of azimuthal vorticities produced at the particle's interface in the presence of shear.

Several works have been devoted to extending Saffman's asymptotic scheme to obtain the lift force on a spherical object moving in shear flow in the low-Reynolds-number regime. These efforts, such as those by McLaughlin (1991) and Legendre & Magnaudet (1997, 1998), refine the asymptotic approach to account for more complex flow conditions. In summary, the analytical solution for the lift coefficient, to the first order, has the following formulation:

$$C_L(Re \ll 1) = \frac{C(\mathcal{R})}{\pi^2} \varepsilon J_L(\varepsilon) - C_L^{(2)}, \quad (4.1)$$

where $\varepsilon = (|Sr|/Re)^{1/2}$ represents the ratio of the Oseen to the Saffman length scales. Here, $C_L^{(2)}$ is the second-order inertial contribution to lift, originally derived by Saffman (1965) as $11Sr/8$ for rigid sphere, with more recent computations by Candelier *et al.* (2023) yielding smaller corrections. The constant C , which will be elaborated in more detail later, depends on the dimensionless parameter $\mathcal{R} = (3\mu^* + 2)/(\mu^* + 1)$ that is the strength of the Stokeslet in the unbounded solution. The term $J_L(\varepsilon)$ denotes a three-dimensional integral that is independent of the droplet's interfacial condition. In the limit as $\varepsilon \rightarrow \infty$, analytical solutions for $J_L(\varepsilon)$ were obtained by Saffman (1965), with $J_L(\infty) = 2.254$. However, the exact manner in which $J_L(\varepsilon)$ approaches $J_L(\infty)$ as ε increases remains analytically unresolved. To solve this, semi-empirical approximations for $J_L(\varepsilon)$ at limited value of ε have been proposed in some studies, given by

$$J_L(\varepsilon) = J_L(\infty)(1 + 0.2\varepsilon^{-2})^{-3/2} \quad (4.2)$$

or $J_L(\varepsilon) = 0.6765 [1 + \tanh[2.5(\lg \varepsilon + 0.191)]] [0.667 + \tan[6(\varepsilon - 0.32)]]$,

where the first correlation was derived through numerical data fitting by Legendre & Magnaudet (1998) and the second correlation was proposed by Mei (1992) based on earlier numerical results provided by McLaughlin (1991). Therefore, both of these approximations for $J_L(\varepsilon)$ are known to be highly dependent on their respective numerical results. Additionally, in the low-but-finite Re regime, it is important to note that the numerical solutions can be significantly affected by the confinement of the computational domain, as reviewed by Shi & Rzehak (2019).

The value of $C(\mathcal{R})$ warrants further discussion. Saffman (1965) derived an analytical value of $C(\mu^* \rightarrow \infty) = 18$ for a rigid sphere. In contrast, Mei & Klausner (1994) reported that $C(\mu^* \rightarrow 0) = C(\mu^* \rightarrow \infty) \cdot \mathcal{R}(\mu^* \rightarrow 0)/\mathcal{R}(\mu^* \rightarrow \infty) = 12$ for an inviscid bubble. Subsequently, Legendre & Magnaudet (1997) challenged this result and provided a more rigorous analysis of C for arbitrary values of μ^* (or \mathcal{R}). They argued that $C(\mathcal{R})$ is proportional to C_{D0}^2 or \mathcal{R}^2 , where C_{D0} is the drag coefficient experienced by the droplet in homogeneous flow at the same Reynolds number. Accordingly, for an inviscid bubble, this implies $C(\mu^* \rightarrow 0) = C(\mu^* \rightarrow \infty) \cdot \mathcal{R}^2(\mu^* \rightarrow 0)/\mathcal{R}^2(\mu^* \rightarrow \infty) = 8$. However, the correlation proposed by Legendre & Magnaudet (1997) for this low-but-finite Reynolds number regime has not yet been validated for droplets with arbitrary μ^* or \mathcal{R} .

Our initial approach involves comparing the present numerical solutions with the aforementioned formulae for varying viscosity ratios μ^* , including (4.1), (4.2), and the proportionality $C(\mathcal{R}) \propto \mathcal{R}^2$. We keep the Reynolds number fixed at $Re = 0.1$. Figure 3(b)

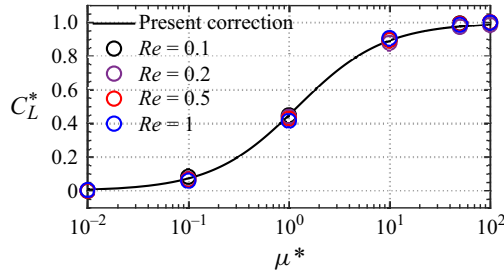


Figure 4. Comparison between numerical results and normalised correlations for C_L on spherical droplets at low-but-finite Re . The numerical data collapse onto a single curve expressed by (4.3) after normalisation.

presents the lift coefficients as a function of the viscosity ratio, while $J_L(\varepsilon)$ is estimated using either (4.2a) (Legendre & Magnaudet 1998) or (4.2b) (Mei 1992). The results show excellent agreement with the theoretical predictions, although they are slightly lower than those predicted by (4.2a), with a discrepancy of less than 5%. This deviation is considered acceptable, as both of the correlations (4.2a) and (4.2b) were derived from numerical data specific to the referenced studies. Similar findings are reported in the recent work by Shi *et al.* (2024) (figure 2 therein), where the ratio of the inner to outer Reynolds number was 5, in contrast to 1 in the present work. Together, these results align with the low- Re analysis conducted by Magnaudet *et al.* (2003), which showed that the hydrodynamic force in the terminal state does not depend on the density ratio (and hence, the Re^*). Furthermore, figure 3(b) illustrates both the pressure and viscous components of the lift coefficients, demonstrating that the viscous component is more dominant than the pressure component in this low-but-finite Reynolds number regime.

Moreover, we try to normalise the lift coefficients with the formulation of $C_L^* = [C_L(Re, \mu^*) - C_L(Re, \mu^* \rightarrow 0)] / [C_L(Re, \mu^* \rightarrow \infty) - C_L(Re, \mu^* \rightarrow 0)]$. If we assume that the correlation $C_L(Re \rightarrow 0, \mu^*) \propto C_{D0}^2(Re \rightarrow 0, \mu^*)$ (Legendre & Magnaudet 1997) holds for spherical droplets in the low-but-finite Re regime, and given that the Oseen formulation can be used to estimate the drag coefficient as $C_{D0}(Re \rightarrow 0, \mu^*) \simeq 8\mathcal{R}/Re$, we derive the following normalised lift in this regime:

$$\begin{aligned}
 C_L^* &= \frac{C_L(Re, \mu^*) - C_L(Re, \mu^* \rightarrow 0)}{C_L(Re, \mu^* \rightarrow \infty) - C_L(Re, \mu^* \rightarrow 0)} = \frac{C_{D0}^2(Re, \mu^*) - C_{D0}^2(Re, \mu^* \rightarrow 0)}{C_{D0}^2(Re, \mu^* \rightarrow \infty) - C_{D0}^2(Re, \mu^* \rightarrow 0)} \\
 &\approx \frac{\left(\frac{8}{Re}\right)^2 [\mathcal{R}(\mu^*)^2 - 2^2]}{\left(\frac{8}{Re}\right)^2 [(3^2 - 2^2)]} \\
 &\approx \frac{(4 + 5\mu^*)\mu^*}{5(1 + \mu^*)^2}. \tag{4.3}
 \end{aligned}$$

This normalised lift coefficient, C_L^* , is compared with our numerical results, as shown in figure 4 for $0.1 \leq Re \leq 1$. Excellent agreement is observed between the theoretical correlation and the numerical data. Thus, this normalised correlation (4.3) effectively predicts the lift force experienced by a spherical droplet in the low-but-finite Re regime. In summary, our numerical results validate the conclusion by Legendre & Magnaudet (1997) that, for a spherical droplet in this regime, the lift force is proportional to the square of the drag force acting on the droplet.

The next step is to explore why the lift force increases with larger μ^* in the low-but-finite Re regime. It is known that the Saffman mechanism is dominant in this regime

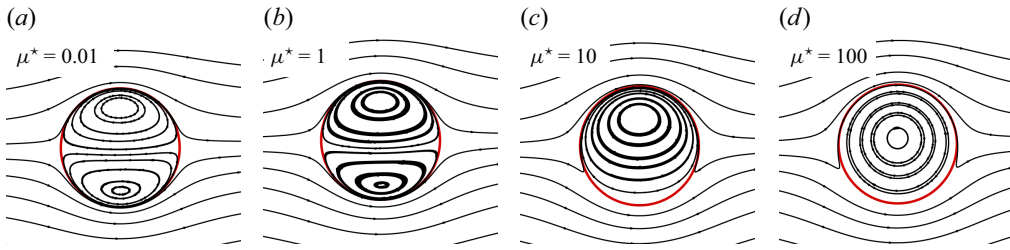


Figure 5. Streamlines internal and external of the droplets at $Re = 0.1$, with the viscosity ratio varying in the range of $0.01 \leq \mu^* \leq 100$. As μ^* increases, a stronger recirculating zone develops on the side with higher velocity past the droplet, thereby generating a more pronounced Saffman mechanism.

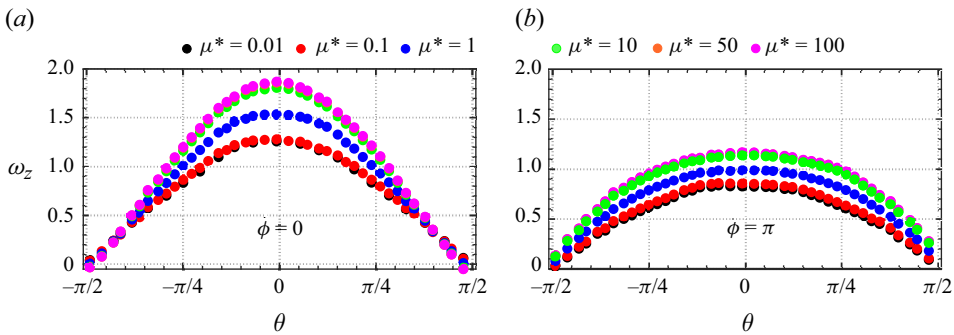


Figure 6. Distribution of ω_z at the (a) top and (b) bottom surfaces of the droplet. A more viscous droplet exhibits a larger $\Delta\omega_\phi = \omega_\phi(\phi = 0) - \omega_\phi(\phi = \pi)$ at the equator, thereby enhancing the Saffman mechanism.

(Legendre & Magnaudet 1997, 1998). This mechanism is associated with the asymmetric advection of azimuthal vorticities generated at the droplet in the presence of shear in the XOY plane. Consequently, it is pertinent to investigate the asymmetric distribution of ω_z (i.e. the projection of ω_ϕ onto the XOY plane) around the spherical droplet as μ^* varies. Figure 5 displays the internal and external streamlines on the XOY plane for different values of μ^* , while maintaining a Reynolds number of $Re = 0.1$. It is evident that a larger μ^* results in a more pronounced recirculating zone on the side with higher velocity past the droplet. This flow structure is consistent with those reported by Ervin & Tryggvason (1997) and Hidman *et al.* (2022), who investigated the rise motion of bubbles in low- Re shear flows. Under these conditions, the negative ω_z observed in the figure is expected to generate a positive lift force $\mathbf{F}_L \cdot \mathbf{e}_y$, given that $\mathbf{F}_L \propto \mathbf{U} \times \boldsymbol{\omega}$. Additionally, a stronger recirculation for larger μ^* leads to a greater lift force. Figure 6 illustrates the distribution of ω_z on the top ($\phi = 0$) and bottom ($\phi = \pi$) surfaces of the droplet, showing the dependence of $\omega_{\phi=0}$ and $\omega_{\phi=\pi}$ on θ . The figure reveals that a more viscous droplet exhibits a larger $\Delta\omega_\phi = \omega_{\phi=0} - \omega_{\phi=\pi}$, confirming that the asymmetric advection of ω_ϕ is responsible for the lift force experienced by the droplet in this low-but-finite Re regime.

4.2. Oblate droplets

We now shift our focus to oblate droplets in the low-but-finite Re regime ($0.1 \leq Re \leq 1$), with aspect ratios varying in the range of $1 \leq \chi \leq 2.5$, which encompasses moderate to high shape deformations. As with spherical droplets discussed in § 4.1, our primary concerns are to understand how and why the lift force evolves with the changing parameters. It is well known that deformable drops and bubbles moving in shear flows can experience lateral migration, even in the zero-Reynolds-number limit, as demonstrated by

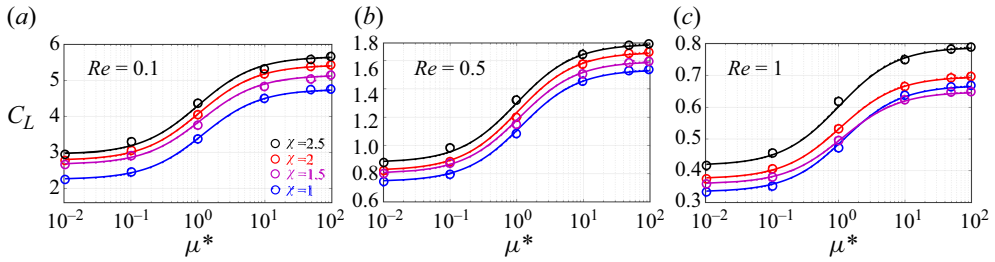


Figure 7. Interpolation scheme for predicting C_L on oblate droplets in the low-but-finite Re regime for (a) $Re = 0.1$, (b) $Re = 0.5$ and (c) $Re = 1$. Points represent numerical results, while the solid lines correspond to the correlation proposed as (4.4).

Leal (1980). Even in the low-Reynolds-number regime, the problem becomes nonlinear due to the fact that the matching of velocities and stresses across the droplet surface must be satisfied on a deformed interface, whose shape is a part of the solution to the problem. Notable contributions to this phenomenon include the works by Chan & Leal (1979) and Magnaudet *et al.* (2003), who analytically solved for the deformation rate of the droplet and the corresponding deformation-induced lift using the reciprocal theorem. Their studies focused on deformation caused by the presence of a wall and shear flow. They found that droplets migrated in a wall-bounded shear flow, with the direction of deformation-induced migration changing with the viscosity ratio, and the migration was directed towards the wall when the viscosity ratio was $\mu^* - O(1)$. In contrast, for an almost inviscid bubble rising in a quiescent liquid, the deformation-induced migration was directed away from the wall, in agreement with experimental results by Takemura *et al.* (2002). Sugiyama & Takemura (2010) also analysed the deformation-induced lift when the bubble was extremely close to the wall. However, the deformation-induced lift force in these studies was derived for a linear shear flow near a wall, where the deformation is somewhat asymmetric compared with the case of an unbounded flow. This differs from the present study, where we assume the deformable droplet maintains an axi-symmetrical shape. The asymmetric deformation of bubbles has been shown to produce a negative lift force in unbounded flow, referred to as the *A*-mechanism (Ervin & Tryggvason 1997; Hidman *et al.* 2022), which acts in the opposite direction to the Saffman mechanism. This effect, however, is beyond the scope of the present study.

Figure 7 illustrates the dependence of $C_L(Re, \mu^*, \chi)$ on μ^* at $Re = 0.1, 0.5$ and 1 , with aspect ratios varying as $\chi = 1.0, \chi = 1.5, 2.0$ and 2.5 in each panel. The first two pictures demonstrate that larger aspect ratios correspond to higher lift coefficients, regardless of the viscosity ratio under consideration. This effect arises because the oblateness of the droplet influences the curvature of the interface and the vorticities generated at the interface are positively correlated with the curvature of the equator. For example, $\omega_{\phi, max} \sim \chi^{8/3}$ for an inviscid oblate bubble (Magnaudet & Mougin 2007). Consequently, the Saffman mechanism is more pronounced for more oblate droplets in this Re regime. In contrast, figure 7(c) shows that at $Re = 1$, the earlier trend – that larger aspect ratios result in higher lift coefficients – largely persists. However, an anomalous reversal is observed for $\mu^* \geq 10$ at $\chi = 1.5$, where the lift force is smaller than that for $\chi = 1.0$. This is not unexpected, as at $(Re, \mu^*) = (5, 100)$, the lift force was already found to decrease monotonically with χ (see figure 12c). This phenomenon can be attributed to the dominance of *S*-mechanism, which generates negative lift on highly viscous droplets. Consequently, the *S*-mechanism may already be present at $Re = 1$, partially offsetting the Saffman mechanism. To substantiate the observation of an intensified Saffman mechanism for oblate droplets, a

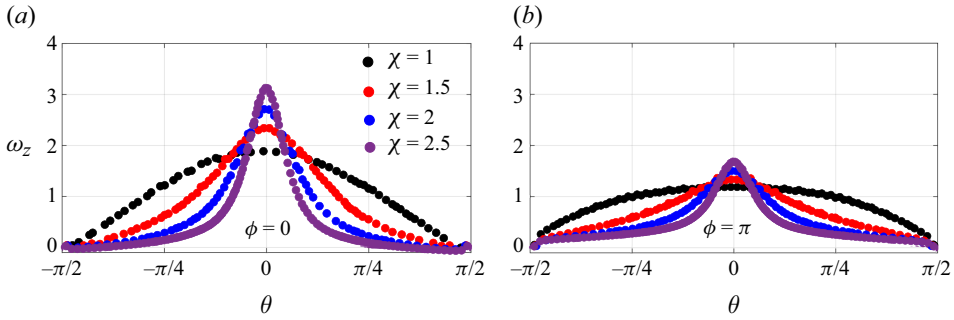


Figure 8. Same plot as in figure 6, with the Reynolds number fixed at $Re = 0.1$ and the viscosity ratio fixed at $\mu^* = 100$, while the aspect ratio of the droplet is varied.

detailed examination of the vorticity distribution around the droplet and its evolution in the flow field is essential. Figure 8 presents the distribution of $\Delta\omega_\phi = (\omega_{\phi=0} - \omega_{\phi=\pi})$ along the droplet interface for different aspect ratios, with Re fixed at 0.1 and viscosity ratio maintained at $\mu^* = 100$. The results confirm that a larger χ enhances the asymmetry of the vorticity at the top ($\phi = 0$) and bottom ($\phi = \pi$) of the droplet, thereby intensifying the Saffman mechanism. Additionally, we aim to develop a semi-empirical correlation to predict $C_L(Re, \mu^*, \chi)$ in this low-but-finite Reynolds number regime for oblate droplets. Although no theoretical work is available for inviscid oblate bubbles or rigid spheroids in this context, we employ an interpolation technique inspired by the correlation established for spherical droplets in (4.3). The following formula is proposed based on this approach:

$$C_L(Re, \mu^*, \chi) = \frac{a\mu^* + b^2}{(\mu^* + b)^2} C_L(Re, \mu^* \rightarrow 0, \chi) + \frac{(\mu^*)^2 + a\mu^*}{(\mu^* + b)^2} C_L(Re, \mu^* \rightarrow \infty, \chi), \tag{4.4}$$

where a and b are coefficients that can be determined empirically. After fitting the numerical results, we find that the coefficients are $a = -0.1954\chi^2 + 0.7833\chi + 0.2730$ and $b = -0.1403\chi^2 + 0.5355\chi + 0.5483$. The validity of this correlation is confirmed by the results presented in figure 7. In this figure, the solid lines corresponding to (4.4) align very well with the numerical data, demonstrating that the proposed correlation effectively captures the variation of lift force with both the viscosity ratio and aspect ratio for spherical to oblate droplets in the low-but-finite Reynolds number regime.

Additionally, it is important to note that in real-world scenarios, a deformable droplet elongates in the extensional direction of the background strain rate and rotates in the rotational direction of the background vorticity. In the low-Reynolds-number regime, the level of asymmetric deformation scales with the capillary number Ca ($Ca = \mu U_\infty / \sigma$, with σ the surface tension coefficient). This deformation-induced lift force scales as $Ca\mu RU_\infty$ (Magnaudet *et al.* 2003). In contrast, the inertial lift force in the presence of shear scales as $(Re Sr)^{1/2} \mu RU_\infty$ implied by (4.1). For the deformation-induced lift to be negligible compared with the inertial lift, the condition $Ca \ll (Re Sr)^{1/2}$ must hold. Since $Sr = 0.2$ is fixed for the majority of the present work and Re values down to 0.1 are considered, the above constraint implies that $Ca \ll 0.1$ is required for the inertial lift to dominate in real-world scenario.

5. Moderate- to high- Re regime

In this section, we examine the lift forces experienced by droplets within the moderate- to high-Reynolds-number regime ($5 \leq Re \leq 300$). This investigation encompasses the

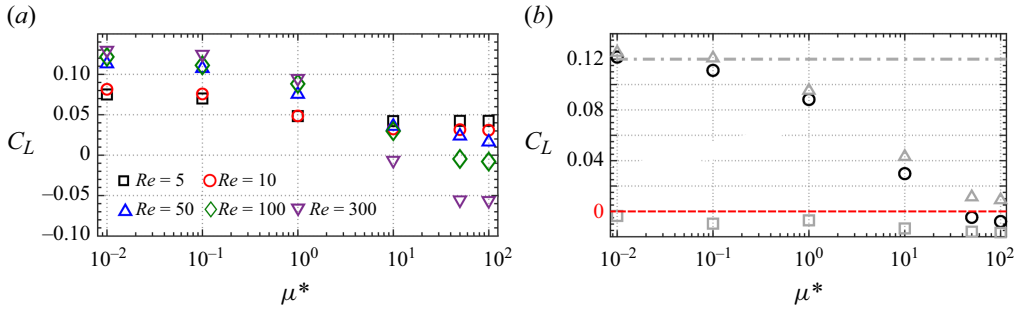


Figure 9. Lift coefficients experienced by spherical droplets in the moderate- to high- Re regime, with variations in Reynolds number and viscosity ratio: (a) C_L versus μ^* for different Re ; (b) C_L versus μ^* with specified $Re = 100$. In panel (b), the dash-dotted line represents the value predicted by correlation (5.1) (Legendre & Magnaudet 1998), the dotted line indicates $C_L = 0$, and the grey triangles and squares denote the pressure and viscous components of the lift coefficients.

transition of the droplet from an inviscid oblate bubble, characterised by $(\mu^*, \chi) = (0.01, 1.0-2.5)$, to a rigid spheroid, with parameters $(\mu^*, \chi) = (100, 1.0-2.5)$. This regime presents a stark contrast to the low-but-finite Reynolds number regime, as the inertial effects become significant and the flow dynamics around the droplet are more complex.

5.1. Spherical droplet

Maintaining the droplet in a spherical shape ($\chi = 1.0$), figure 9(a) illustrates the variation of lift coefficient C_L with viscosity ratio μ^* across different Reynolds numbers Re . For highly viscous droplets, the lift coefficient may exhibit unsteady behaviour due to vortex shedding, therefore, the time-averaged C_L is presented in the figure for those unsteady scenarios. It is observed that $C_L(Re, \mu^*)$ decreases with increasing μ^* and can even turn negative for high-Reynolds-number droplets ($Re \geq 100$) at viscosity ratio exceeding a certain critical value. The same trend has been reported by Shi *et al.* (2024) (figures 4 and 5 therein), where the critical viscosity ratio depends only weakly on the Reynolds number ratio. This behaviour suggests a fundamental shift in the lift generation mechanism between the moderate- to high- and low-but-finite Reynolds number regimes. Focusing on spherical droplets at $Re = 100$, figure 9(b) shows the dependence of lift coefficients on μ^* . A sign reversal in the lift coefficient is noted within the range $10 < \mu^* < 50$. The figure also displays the pressure and viscous components of the lift force. It is evident that the viscous component is negative across all viscosity ratios, while the positive pressure component decreases with μ^* until it becomes smaller than the magnitude of the negative viscous component. This trend indicates that viscous effects dominate and lead to a reversal of the net lift force for viscous droplets in the moderate- to high-Reynolds-number regime. This negative contribution of the viscous component to lift has been reported previously by Legendre & Magnaudet (1998) and Kurose *et al.* (2001) for inviscid bubbles, as well as by Sugioka & Komori (2007) and Bagchi & Balachandar (2002) for water/rigid spheres. Additionally, Legendre & Magnaudet (1998) proposed an empirical correlation for predicting the lift coefficient of an inviscid spherical bubble in this moderate- to high-Reynolds-number regime, given by

$$C_L(Re, \mu^* \rightarrow 0, \chi = 1.0) = \frac{2Sr}{3} \frac{1 + 16Re^{-1}}{1 + 29Re^{-1}}. \quad (5.1)$$

According to this correlation, the predicted lift coefficient for $Re = 100$ and $\mu^* \rightarrow 0$ is approximately 0.12, as indicated by the dash-dotted line in [figure 9\(b\)](#). This value is in excellent agreement with our numerical results at $\mu^* = 0.01$. Conversely, we have not included reference data for the case of a rigid sphere ($\mu^* = 100$) due to the variability in available direct numerical simulation results for this Reynolds number (Shi & Rzehak 2019). The negative lift coefficient observed for $Re = 100$ and $\mu^* \rightarrow \infty$ is notably sensitive to the shear rate and the specific numerical settings employed in different simulations. The reported values in different numerical simulations and the corresponding numerical settings are summarised in [Appendix B](#), where the information on the parameter choices, grid resolutions and boundary conditions is provided.

To investigate the mechanism underlying the lift reversal observed in [figure 9](#) and the dependency of C_L on μ^* , we first consider the lift generation mechanisms in inviscid shear flow. In such a flow, the lift force arises from the advection and stretching of the basic vorticity, represented by $\omega_z = \alpha e_z$ in the unperturbed shear flow. The asymmetric stretching of ω_z , characterised by $\omega_z \partial U_x / \partial z$ due to the presence of a spherical droplet, results in a pair of counter-rotating streamwise vortices in the wake (Lighthill 1956; Auton 1987; Auton *et al.* 1988). These vortices induce a positive lift force directed towards the side with the higher velocity, a mechanism known as the *L*-mechanism (Adoua *et al.* 2009). This mechanism has been confirmed by Legendre & Magnaudet (1998) and Adoua *et al.* (2009) for inviscid bubbles in the moderate- to high-Reynolds-number regime.

Additionally, it is important to consider another source of counter-rotating streamwise vortices, which arises from the asymmetric advection of the azimuthal vorticity ω_ϕ generated at the body surface. In the presence of shear, the stretching and tilting of ω_ϕ , represented by $\omega_\phi \partial U_x / \partial \phi$, lead to the formation of counter-rotating streamwise vortices that produce a negative lift force directed towards the side with the lower velocity. This mechanism, referred to as the *S*-mechanism (Adoua *et al.* 2009), becomes dominant for highly deformed bubbles where $\omega_{\phi, max}$ increases proportionally to $\chi^{8/3}$ (Magnaudet & Mougin 2007), as discussed by Adoua *et al.* (2009) and Hidman *et al.* (2022). Furthermore, increasing the viscosity of the droplet, represented by a higher μ^* , may lead to the formation of attached eddies in the droplet's wake due to flow separation. Rachih *et al.* (2020) demonstrate that such attached eddies form at Reynolds numbers of approximately 25 for homogeneous flow past a droplet with $\mu^* > 10$. In the presence of shear, the inhomogeneous flow disrupts the axisymmetry of these attached eddies, causing them to tilt and generate counter-rotating streamwise vortices through the stretching and tilting effects in the vorticity equations. These streamwise vortices contribute to a negative lift force on the droplet and represent a specific case of the *S*-mechanism. Thus, in the following study, we will also attribute such tilting eddy-induced lift to the *S*-mechanism.

Consequently, the fundamental distinction between the *L*-mechanism and the *S*-mechanism lies in their origins of streamwise vorticity. In the *L*-mechanism, the streamwise vorticity is generated from ω_z present in the upstream shear flow, while in the *S*-mechanism, it originates from ω_ϕ produced at the droplet's interface. Referring to [figure 9\(b\)](#), it is evident that an increase in the viscosity ratio μ^* leads to a significant rise in ω_ϕ at the interface, thereby making a transition of dominance from the *L*- to *S*-mechanism. This transition results in a decrease in lift, potentially reversing it from positive to negative values. Additionally, in the scenario dominated by the tilting of the azimuthal vorticity, the lift force is influenced not only by the counter-rotating streamwise vortices (associated with the previously mentioned *S*-mechanism) but also by the asymmetric advection of azimuthal vorticities. This latter effect is referred to as the 'extended Saffman mechanism' in the moderate- to high-*Re* regime because it shares some similarities with the Saffman mechanism dominating in the low-*Re* regime. However, it is important to emphasise

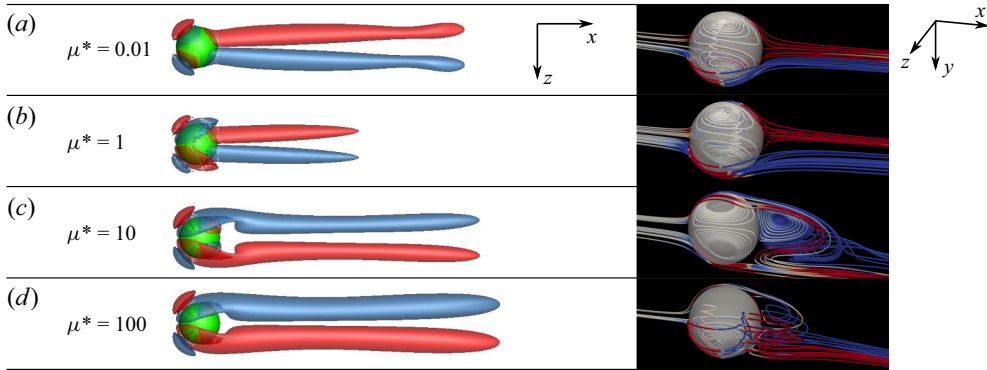


Figure 10. Flow patterns past spherical droplets of $Re = 100$ with varying viscosity ratios: (a) $\mu^* = 0.01$; (b) $\mu^* = 1$; (c) $\mu^* = 10$; (d) $\mu^* = 100$. For each viscosity ratio, the left panel displays the iso-surfaces of streamwise vorticity $\omega_x = \pm 0.3$ in the wake of the droplet, while the right panel illustrates the three-dimensional streamlines, with colour indicating ω_x values ranging from -0.3 (blue) to 0.3 (red). In the right panels, attached eddies appear and are tilted at $\mu^* \geq 10$.

that the Saffman and extended Saffman mechanisms are fundamentally different from a mathematical perspective. as we point out in § 4.1 that the Saffman mechanism is rooted in an asymptotic approach, which no longer applies in the moderate- to high-Reynolds-number regime. In this regime, the radius of the Stokes region becomes small, making it impossible to distinguish between inner and outer regions. Since these two mechanisms, arising from azimuthal vorticity, produce opposing effects on the lift – positive lift from the extended Saffman mechanism and negative lift from the S -mechanism – they tend to counter balance each other, particularly for highly viscous droplets.

To investigate the transition from the L -mechanism to the S -mechanism as μ^* increases in the moderate- to high-Reynolds-number regime, we examine the streamwise vortices $\omega_x = \pm 0.3$ in the wake of droplets, with the Reynolds number maintained at $Re = 100$. The left panels of figure 10 illustrate these vortices. For weakly to moderately viscous droplets at $\mu^* = 0.01$ and 1 , where the L -mechanism is predominant, the produced ω_x exhibits positive values at $z < 0$ and negative values at $z > 0$. Consequently, the fluid situated between these vortices is entrained inwards ($y < 0$), generating a positive counteracting lift on the droplet, consistent with the observations in figure 9(b). In contrast, for moderately to highly viscous droplets $\mu^* = 10$ and 100 , the signs of ω_x reverse compared with the cases with lower viscosity ratios, indicating a shift to the S -mechanism. The right panels of figure 10 show that at these higher viscosity ratios, attached eddies form in the wake of the droplet and become tilted due to the ambient shear. This tilting generates streamwise vortices consistent with the S -mechanism. Unlike in homogeneous flow, where the direction of the lift force can be influenced by random disturbances (Johnson & Patel 1999; Thompson *et al.* 2001), the shear in the present case acts as a controlled disturbance that consistently tilts the eddies in the y -direction, thus producing a lift in the same direction. Additionally, Rachih *et al.* (2020) demonstrated that at $Re = 100$, the formation of attached eddies behind the droplet occurs only when the viscosity ratio exceeds $\mu^* > 5$. This finding is in agreement with our observations presented in figure 10.

It is noteworthy that although the counter-rotating streamwise vortices at $\mu^* = 10$ and 100 share the same sign, the corresponding lift forces on the droplets exhibit opposite signs – specifically, a positive C_L for $\mu^* = 10$ and a negative C_L for $\mu^* = 100$ (see figure 9b). This observation suggests that the reversal of lift force lags behind the reversal of streamwise vortices, indicating that the lift in this transitional regime is not solely

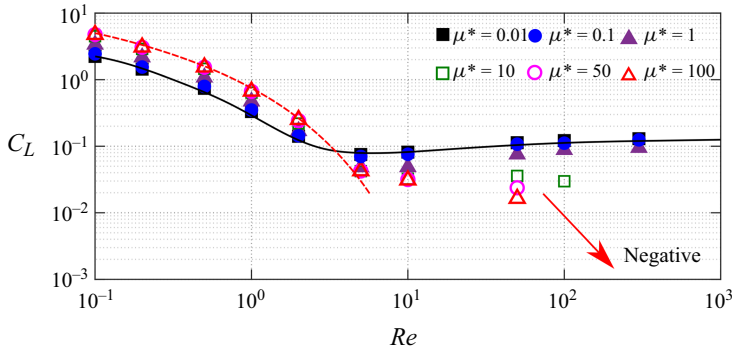


Figure 11. Variation of the lift coefficient C_L with Reynolds number ranging from low to moderately high values for spherical droplets. The solid line represents the correlation $C_L(Re, Sr) = ([C_L^{low Re}(Re, Sr)]^2 + [C_L^{high Re}(Re, Sr)]^2)^{1/2}$ proposed by Legendre & Magnaudet (1998) for spherical bubbles. The dashed line denotes the correlation $C_L(Re, Sr) = 2.518J_L(\varepsilon)(\alpha/Re)^{1/2}$ suggested by McLaughlin (1991) for rigid spheres at low-but-finite Re , with $J_L(\varepsilon)$ being estimated by (4.2b).

determined by the sign of the streamwise vorticities. This scenario contrasts with the well-understood behaviour in homogeneous flow past blunt bodies, where the streamwise vortices in the wake predominantly dictate the direction of lift, whether for an oblate bubble (Magnaudet & Mougin 2007; Zhang & Ni 2017) or a rigid sphere (Johnson & Patel 1999; Thompson *et al.* 2001). Hence, an additional mechanism must be at play to account for the positive lift observed at $\mu^* = 10$. This positive lift could counterbalance the negative lift induced by the S -mechanism, resulting in a net positive lift. As conjectured earlier, this ‘positive’ lift may be attributed to the asymmetric advection of azimuthal vorticities, which is termed the extended Saffman mechanism and becomes significant at higher viscosity ratios. We will explore this hypothesis further in § 6, employing a force decomposition method grounded in the theory of vorticity moments to quantitatively analyse this effect.

Next, we examine the influence of Reynolds number on the lift coefficient across the entire low- to moderately high- Re regime. Figure 11 illustrates the dependency of C_L on Re . For clarity, the graph is presented on a logarithmic scale, with negative values of C_L not shown but indicated by an inset arrow. The figure includes the correlation proposed by Legendre & Magnaudet (1998) (black solid line), given by $C_L(Re, Sr) = ([C_L^{low Re}(Re, Sr)]^2 + [C_L^{high Re}(Re, Sr)]^2)^{1/2}$, where $C_L^{low Re}(Re, Sr)$ is predicted using (4.1) and (4.2a), and $C_L^{high Re}(Re, Sr)$ is computed from (5.1). This correlation effectively predicts C_L for inviscid bubbles and shows excellent agreement with the present results across the full parameter space, from the Saffman mechanism to the regime dominated by the L -mechanism. Specifically, C_L initially decreases with Re until a critical value of $Re \approx 5$, due to the weakening of the Saffman mechanism, and then increases as the L -mechanism becomes more influential with increasing inertial effects. This trend is consistent with the numerical findings of Legendre & Magnaudet (1998) and Kurose *et al.* (2001), and is also applicable to weakly to moderately viscous droplets with $\mu^* \leq 10$. Additionally, the correlation proposed by McLaughlin (1991) (red dashed line), given by $C_L(Re, Sr) = 2.518J_L(\varepsilon)(\alpha/Re)^{1/2}$ where $J_L(\varepsilon)$ is estimated by (4.2b), is used to model the lift coefficient for a rigid sphere. This model aligns with our numerical data up to $Re \approx 5$. For moderately to highly viscous droplets ($\mu^* \geq 10$), we observe a monotonic decline in C_L with increasing Re , attributed to the dominance of the S -mechanism which

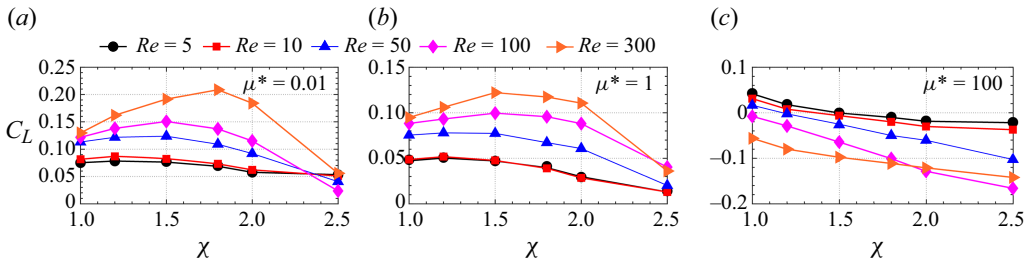


Figure 12. Evolution of lift coefficients with aspect ratio in the moderate- to high-Reynolds-number regime: (a) inviscid bubble with $\mu^* = 0.01$; (b) droplet with $\mu^* = 1$; (c) rigid spheroid with $\mu^* = 100$.

reduces and can even reverse the lift. However, Rachih *et al.* (2020) indicates that attached eddies form in the wake of the droplet at $(Re, \mu^*) \approx (50, 50)$. Beyond this point, the shear tends to tilt the eddies, potentially reversing the streamwise vorticities and making negative lift more probable. Despite this, positive lift is still observed from our data displayed in figure 11, again suggesting the presence of an additional mechanism contributing extra positive lift.

5.2. Oblate droplet

We now examine the behaviour of oblate droplets in the moderate- to high-Reynolds-number regime. Figure 12 presents the lift coefficient C_L for oblate droplets with aspect ratios $1.0 \leq \chi \leq 2.5$, with viscosity ratios $\mu^* = 0.01, 1$ and 100 depicted in separate panels. For cases where the lift coefficient is unsteady, such as for oblate bubble at $(Re, \mu^*, \chi) = (300, 0.01, 2.5)$ and for rigid sphere at $(Re, \mu^*, \chi) = (300, 100, 1.0)$, we still use time-averaged values of C_L . For inviscid bubbles ($\mu^* = 0.01$), figure 12(a) shows that at $Re = 5$ and 10 , C_L decreases monotonically with increasing χ . This trend is attributed to the fact that the L -mechanism does not dominate at this moderate Reynolds number and the increase in oblateness strengthens the S -mechanism, thereby reducing the positive value of the lift. As the Reynolds number increases to $Re \geq 50$, C_L initially increases with χ until it reaches a Reynolds-number-dependent threshold, χ_{cr} . For $Re = 50$ and 100 , χ_{cr} is approximately 1.5 , while for $Re = 300$, χ_{cr} is approximately 1.8 . Beyond this critical aspect ratio, C_L begins to decrease with increasing χ . To understand this non-monotonic dependence of C_L on χ , we must consider the interplay between the S -mechanism and the L -mechanism for oblate bubbles. According to Naciri (1992), for inviscid shear flow around a body, such as a potential flow past an oblate bubble, $C_L(Re \rightarrow \infty, \mu^* \rightarrow 0, \chi)$ closely mirrors the added mass coefficient and thus increases with aspect ratio. This theoretical prediction was numerically validated by Adoua *et al.* (2009) at very high Reynolds numbers ($Re \approx 4 \times 10^3$) and is also supported by our numerical data presented in Appendix A. However, at moderate to high Reynolds numbers ($Re \leq 15 \times 10^3$), Adoua *et al.* (2009) also observed that $C_L(Re, \mu^* \rightarrow 0, \chi)$ does not always increase with χ , but can decline after reaching a critical threshold χ_{cr} , consistent with our numerical results. This behaviour arises because the enhanced S -mechanism grows faster than the L -mechanism when $\chi > \chi_{cr}$. Figure 12(b) presents results for droplets with $\mu^* = 1$, where the variation in C_L with χ follows a similar trend to that observed for $\mu^* = 0.01$. This suggests that the L - and S -mechanisms exhibit comparable dominating regimes for droplets with $\mu^* = 0.01$ and $\mu^* = 1$. For droplets with higher viscosity ratios, corresponding to rigid spheroids ($\mu^* = 100$), figure 12(c) shows that C_L consistently decreases with χ and may even become negative. This outcome indicates that

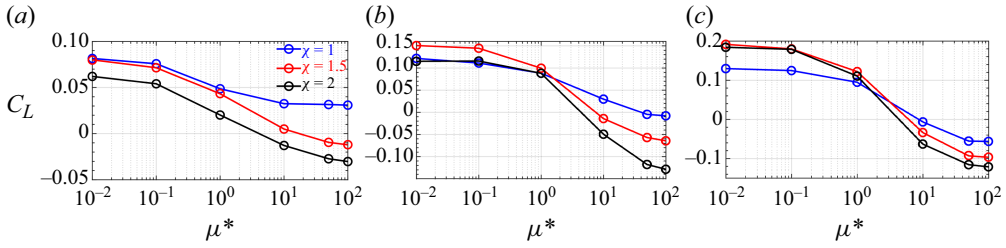


Figure 13. Evolution of lift coefficients with viscosity ratio and aspect ratio in the moderate- to high-Reynolds-number regime: (a) $Re = 10$; (b) $Re = 100$; (c) $Re = 300$.

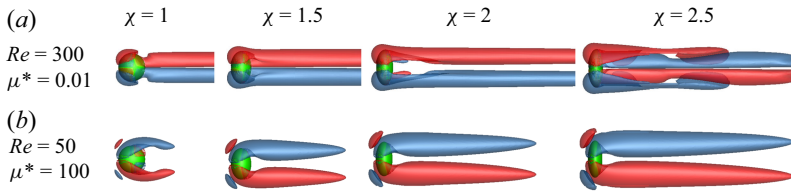


Figure 14. Counter-rotating streamwise vortices behind the droplet at different aspect ratios, with iso-surfaces corresponding to $\omega_x = \pm 0.3$: (a) inviscid oblate bubbles with $(Re, \mu^*) = (300, 0.01)$; (b) rigid spheroids with $(Re, \mu^*) = (50, 100)$.

the S -mechanism predominates for such highly viscous droplets, leading to a reduction in C_L as the droplet deformation increases.

We now explore the dependency of C_L on μ^* for droplets with different oblateness. Figure 13 presents the numerical results for different Reynolds numbers: $Re = 10, 100$ and 300 . In figure 13(a), at $Re = 10$, it is evident that the lift coefficient C_L decreases both with χ and with μ^* . This behaviour is attributed to the enhanced S -mechanism associated with increasing μ^* , as previously discussed. At higher Reynolds numbers, specifically $Re = 100$ and 300 , figures 13(b) and 13(c) show that C_L consistently declines with μ^* for a given aspect ratio, similar to observations for spherical droplets. However, the relationship between C_L and aspect ratio χ varies significantly depending on the viscosity ratio μ^* . For weakly to moderately viscous droplets ($0.01 \leq \mu^* \leq 1$), the variation of C_L with χ is non-monotonic. In contrast, for moderately to highly viscous droplets ($1 \leq \mu^* \leq 100$), C_L decreases monotonically with χ . The differing impacts of χ in these two viscosity regimes can be explained by the roles of the L - and S -mechanisms. While the S -mechanism not only strengthens with increasing μ^* but also intensifies with χ , the L -mechanism grows with χ up to a certain threshold for weakly to moderately viscous droplets, but always decreases with χ for moderately to highly viscous droplets. Consequently, for droplets with $\mu^* \leq 1$, the effect of χ on C_L is complex due to the concurrent influences of both L - and S -mechanisms. Conversely, for droplets with $\mu^* > 1$, where the S -mechanism predominates, C_L is expected to have a purely negative relationship with χ .

As previously discussed in § 5.1, the L - and S -mechanisms generate opposing streamwise vortices, resulting in reversed lift forces. To further elucidate these vortex structures behind oblate droplets in different regimes, we examine the iso-surfaces of $\omega_x = \pm 0.3$ in the wake of oblate droplets. Figure 14(a) illustrates these iso-surfaces for bubbles with $(Re, \mu^*) = (300, 0.01)$ across varying aspect ratios, $1 \leq \chi \leq 2.5$. For weakly to moderately deformed bubbles ($1 \leq \chi \leq 1.5$), which fall under the regime dominated by the L -mechanism, a pair of counter-rotating streamwise vortices produces a positive lift. However, as the aspect ratio increases to $\chi = 2.0$, a second pair of

vortices with opposite signs begins to emerge on the inner side of the wake. This additional pair of vortices is associated with the *S*-mechanism, specifically the tilting of attached eddies that develop beyond a critical aspect ratio of $\chi \approx 1.75$ (Blanco & Magnaudet 1995; Magnaudet & Mougin 2007). As χ increases to 2.5, the *S*-mechanism intensifies, leading to negative lift that partially offsets the positive lift generated by the *L*-mechanism. This explains the observed decrease in C_L for $\chi > 1.8$, as shown in figure 12(a). For rigid spheroids at $(Re, \mu^*) = (50, 100)$, with aspect ratios varying in the range of $1 \leq \chi \leq 2.5$, figure 14(b) depicts the iso-surfaces of the streamwise vortices. In this case, ω_x does not change sign with increasing χ , rather, it is consistently produced by the tilting of the attached eddies. Notably, figure 12(c) reveals that negative C_L is observed only for $\chi \geq 1.2$, while C_L remains positive for $\chi = 1.0$. This discrepancy, again, indicates that the reversal of the lift force lags behind the reversal of the streamwise vortices. Thus, there must be an additional mechanism contributing to the positive lift that counteracts part of the negative lift induced by the *S*-mechanism. We will address this further in § 6, where we demonstrate that the asymmetric distribution of azimuthal vorticities is responsible for this additional positive lift.

6. Mechanism for the lift reversal

Thus, we obtain a comprehensive understanding of the lift evolution on viscous droplets based on the numerical results provided above. In the low-but-finite Reynolds number regime ($Re \leq 1$), both the aspect ratio χ and the viscosity ratio μ^* enhance the Saffman mechanism, which generates a positive lift force. Consequently, in this regime, the lift coefficient C_L increases with both μ^* and χ . As we transition to the moderate-Reynolds-number regime ($1 < Re \leq 10$), the Saffman mechanism diminishes while the *S*-mechanism gains prominence with increasing μ^* and χ . This shift results in a decrease in C_L with both χ and μ^* , with the coefficient C_L potentially becoming negative for highly viscous and highly deformed droplets. In the moderate- to high-Reynolds-number regime ($10 < Re \leq 300$), the *L*-mechanism becomes more significant for weakly to moderately viscous droplets. In this case, C_L increases with χ until it reaches a Reynolds-number-dependent threshold, χ_{cr} . Beyond this critical aspect ratio χ_{cr} , or for droplets that are either highly viscous or highly deformed ($\chi > \chi_{cr}$), the *S*-mechanism prevails, leading to a reduction or even reversal of the lift force.

In what follows, we provide a more quantitative analysis of lift reversal in the moderate-to high-Reynolds-number regime. Our focus is on elucidating the relationship between lift variation and the counter-rotating streamwise vorticities appearing in the shear flow. Additionally, we explore the influence of the shear rate on lift reversal. It is important to note again that an in-depth investigation into the effects of the ratio of the Reynolds number (Re^*) is outside the scope of this study, while a brief discussion on this topic is provided in Appendix E.

6.1. Lift dependency on the counter-rotating streamwise vortices

From the wake structures presented in figures 10 and 14, we observe that in the moderate-to high-Reynolds-number regime, the lift force on a droplet in shear flow is closely related to the signs of the counter-rotating streamwise vortices. These vortices can arise from either the *L*- or *S*-mechanism. However, the reversal of lift, induced by increasing μ^* or χ , occurs with a delay relative to the sign reversal of these vortices. This discrepancy is attributed to an undetermined mechanism, which contributes a positive lift that partially offsets the negative lift generated by the *S*-mechanism.

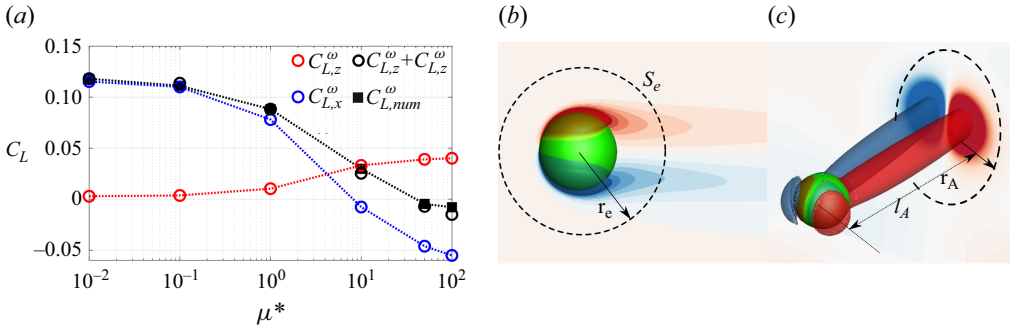


Figure 15. Decomposition of vorticity forces using (6.1), with droplets having fixed parameters of $(Re, \chi) = (100, 1.0)$. (a) Evolution of vorticity forces with respect to the viscosity ratio μ^* . Here, $C_{L,z}^\omega$ is less significant for weakly to moderately viscous droplets, but becomes more important for moderately to highly viscous droplets. (b) Integration domain for computing F_{L,ω_z} using (6.1a), and the iso-contours represent $-0.3 \leq \omega_z \leq 0.3$, with $r_e = 4R$ indicating the outer radius of Ω_e used in the integration. (c) Integration domain for computing F_{L,ω_x} using (6.1b), and the iso-surfaces correspond to $\omega_x = \pm 0.3$, with $l_A = 14R$ being the distance from A_{wake} to the droplet centre and $r_A = 4.4R$ representing the radius for area integration.

To confirm this, we conduct a quantitative analysis based on the theory of vorticity dynamics (Saffman 1995; Wu *et al.* 2007b). This framework indicates that the total force acting on a body moving through a viscous flow arises from body-induced vorticity moments. This theoretical approach has been successfully applied to study solid–fluid interactions (Wu *et al.* 2005, 2007a; Wang *et al.* 2019; Tong *et al.* 2021). More recently, Hidman *et al.* (2022) employed this vorticity-based approach to evaluate the lift force on a freely rising bubble in a shear flow, finding strong agreement with numerical results from a force-balanced model based on bubble motion dynamics. In this section, we apply a rigorous force decomposition using vorticity moments to elucidate the precise origins of the lift experienced by the droplet.

The lift forces F_L parallel to \mathbf{e}_y can be decomposed into two components: one arising from the z -component azimuthal vorticity ω_z and the other from the x -component streamwise vorticity ω_x . The detailed derivations of these vorticity forces, based on the theory of vorticity moments, are presented in Appendix C. Note that these derivations are based on the Cartesian coordinate system rather than the cylindrical system, as both the flow shear and the induced lift force are aligned with the y -direction, making the use of the Cartesian coordinate system more convenient for these investigations. As depicted in figure 15(b), the approximate expressions for the lift forces due to ω_z and ω_x can be formulated as

$$F_{L,z}^\omega = -\frac{1}{2} \left(\rho_l U_x \int_{\Omega_i + \Omega_e} \omega_z d\Omega + \int_{S_e} \omega_z x \mathbf{u} \cdot \mathbf{n} dS \right), \quad (6.1)$$

$$F_{L,x}^\omega = \frac{1}{2} \rho_l U_x \int_{A_{wake}} \omega_x z dA.$$

Here, Ω_i represents the volume of the internal fluid occupied by the droplet, Ω_e is the volume of the external fluid surrounding the droplet and S_e denotes the outer boundary of Ω_e . The term $\mathbf{u} \cdot \mathbf{n}$ refers to the normal velocity on S_e . Additionally, U_x is the imposed velocity in the x -direction, and A_{wake} is the cross-sectional area downstream of the droplet, where $\omega_x dA$ represents the flux of the streamwise vorticities through the cross-section. For $F_{L,z}^\omega$, the combination of the volume and surface integrals ensures that the formulation remains conservative, making the specific choice of Ω_e less critical. In

contrast, for $F_{L,x}^\omega$, the selection of A_{wake} downstream of the droplet is crucial. We have conducted a thorough study to ensure that the results are independent of the choice of A_{wake} and the details of this study are presented in [Appendix C](#). Note that the formulations in (6.1) are simplified for steady-flow conditions, so that scenarios involving vortex shedding are not addressed in this section. In addition, (6.1b) is exactly the formulation proposed by Zenit & Magnaudet (2009) for lift force estimation on a zig-zagging bubble in experiments, while $\int \omega_x dA$ denotes the strength of the circulation of the vortex threads.

The first set of numerical cases we investigate is $(Re, \chi) = (100, 1.0)$, with the viscosity ratio varying in the range of $0.01 \leq \mu^* \leq 100$, as examined in § 5.1 (see [figure 9b](#)). We observe a continuous decrease in C_L with increasing μ^* , which eventually reverses at a viscosity ratio greater than $\mu^* = 10$. Notably, the counter-rotating streamwise vortices change signs before reaching $\mu^* = 10$ (see [figure 10](#)). We compute the vorticity forces based on (6.1), with the results presented in [figure 15\(a\)](#). The lift coefficient $C_{L,num}$, obtained from pressure and viscous integration (2.4), is shown by black squares. The components $C_{L,x}^\omega$ (blue circle) and $C_{L,z}^\omega$ (red circle) are computed using the vorticity moment method, with their combined sum, $(C_{L,x}^\omega + C_{L,z}^\omega)$, indicated by the black circle. For $\mu^* = 0.01$, [figure 15\(b\)](#) shows the distribution of $-0.3 \leq \omega_z \leq 0.3$ on the XOY plane around the droplet, where $r_e = 4R$ represents the outer radius of Ω_e used for integration. [Figure 15\(c\)](#) displays the iso-surfaces of $\omega_x = \pm 0.3$ in the droplet's wake, with $l_A = 14R$ being the distance between A_{wake} and the droplet centre, and $r_A = 4.4R$ as the corresponding radius for area integration. [Appendix C](#) confirms that the choices of l_A and r_A have already converged.

[Figure 15\(a\)](#) shows that, for any μ^* , the sum of $C_{L,x}^\omega$ and $C_{L,z}^\omega$, i.e. $(C_{L,x}^\omega + C_{L,z}^\omega)$, aligns very closely with $C_{L,num}$. This agreement validates the credibility of the force computation based on the vorticity moment in (6.1). It should still be noted that a slight discrepancy between the values of $C_{L,num}$ and $(C_{L,x}^\omega + C_{L,z}^\omega)$ is observed at high μ^* , especially for $\mu^* = 100$. This discrepancy arises because the formulation in (6.1) is an approximation using the vorticity moment method, with further details discussed in [Appendix C](#). [Figure 15\(a\)](#) also reveals that, for weakly to moderately viscous droplets ($\mu^* \leq 1$), $C_{L,x}^\omega$ is almost equal to $C_{L,num}$, while $C_{L,z}^\omega$ is positive but negligible. This strongly suggests that, in this μ^* regime, nearly all the lift originates from the streamwise vortices generated by the L -mechanism. However, as μ^* increases, the vorticity forces produced by ω_z grow sharply, corresponding to positive values, causing $C_{L,x}^\omega$ to deviate from $C_{L,num}$. In particular, at $\mu^* = 10$, $C_{L,x}^\omega$ is a small negative value of -5×10^{-3} , compared with the positive lift of $C_{L,num} = 3 \times 10^{-2}$. This deviation occurs because $C_{L,z}^\omega$ increases to 3.5×10^{-2} , contributing more to the total lift. Consequently, the force decomposition explains why the streamwise vortices change sign at $\mu^* = 10$, yet the lift remains positive, addressing the question raised in the description of [figure 10](#). This demonstrates that, in the moderate- to high- Re regime for a moderately to highly viscous droplet, where the S -mechanism becomes dominant, even if the S -mechanism generates streamwise vortices that produce negative lift, the asymmetric distribution of ω_z in terms of the ‘extended Saffman mechanism’ may contribute more to the lift than ω_x , allowing the total lift to remain positive. As the viscosity ratio further increases to $\mu^* = 50$ and 100, the streamwise vorticity-induced lift coefficient approaches $C_{L,x}^\omega = -5 \times 10^{-2}$, while the total lift is $C_{L,num} = -5 \times 10^{-3}$. This is because the positive lift generated by asymmetric ω_z also rises to $C_{L,z}^\omega = 4.5 \times 10^{-2}$, offsetting most of the negative $C_{L,x}^\omega$.

Furthermore, the contribution of $C_{L,z}^\omega$ becomes more pronounced at higher values of μ^* , as the azimuthal vorticity generated around the droplet increases with μ^* . This

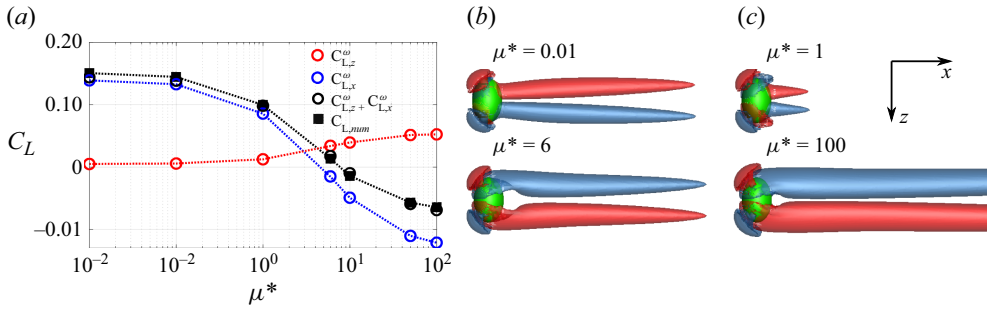


Figure 16. Decomposition of vorticity forces using (6.1), with droplets having fixed parameters of $(Re, \chi) = (100, 1.5)$. (a) Evolution of the vorticity forces with respect to the viscosity ratio μ^* . (b) Iso-surfaces of $\omega_x = \pm 0.3$ for different viscosity ratios μ^* . The results reveal that $C_{L,z}^\omega$ is less significant for weakly to moderately viscous droplets but becomes more important for moderately to highly viscous droplets. Additionally, focusing on the case of $\mu^* = 6$ reveals that the sign reversal of the lift lags behind the sign reversal of ω_x .

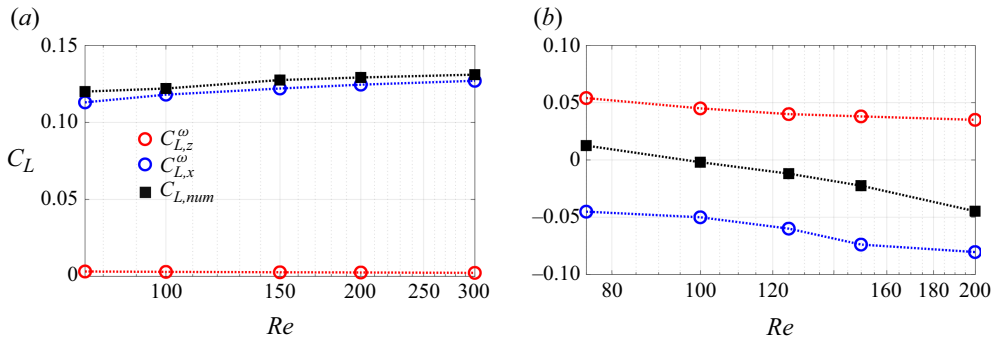


Figure 17. Evolution of the vorticity forces as a function of Reynolds number. (a) Results for spherical bubbles with parameters $(\mu^*, \chi) = (0.01, 1.0)$. (b) Results for rigid spheres with parameters $(\mu, \chi) = (100, 1.0)$.

results in a more intense asymmetric convection of ω_z . This observation highlights a key difference from homogeneous flows past highly viscous droplets or rigid spheres, where the direction of the lateral lift force is predominantly determined by the counter-rotating streamwise vortices alone. In contrast, in shear flow, the streamwise vortices cannot solely dictate the magnitude or direction of the lift force because the azimuthal vortices also play a significant role. Additionally, figure 16 presents results for oblate droplets with $(Re, \chi) = (100, 1.5)$. A similar trend is observed in the variation of C_L with respect to μ^* . For weakly to moderately viscous droplets ($\mu^* \leq 1$), the lift coefficient $C_{L,num}$ is predominantly influenced by $C_{L,x}^\omega$. However, for moderately to highly viscous droplets ($\mu^* \geq 1$), the influence of $C_{L,z}^\omega$ becomes significant. Figure 16(b) illustrates that the sign reversal of the streamwise vortices occurs at $\mu^* = 6$, leading to a negative $C_{L,x}^\omega$. Despite this, the total lift coefficient $C_{L,num}$ remains positive at $\mu^* = 6$, as shown in figure 16(a), due to the positive contribution of $C_{L,z}^\omega$.

We further examine how $C_{L,x}^\omega$ and $C_{L,z}^\omega$ vary with the Reynolds number, keeping other parameters constant. This analysis includes both spherical bubbles and rigid spheres. For spherical bubbles, with parameters fixed at $(\mu^*, \chi) = (0.01, 1.0)$, we vary the Reynolds number in the range of $50 \leq Re \leq 300$ and the results are presented in figure 17(a). It is evident that across all Reynolds numbers considered, $C_{L,x}^\omega$ aligns closely with $C_{L,num}$, while $C_{L,z}^\omega$ remains positive and negligible, decreasing with μ^* . This indicates that the

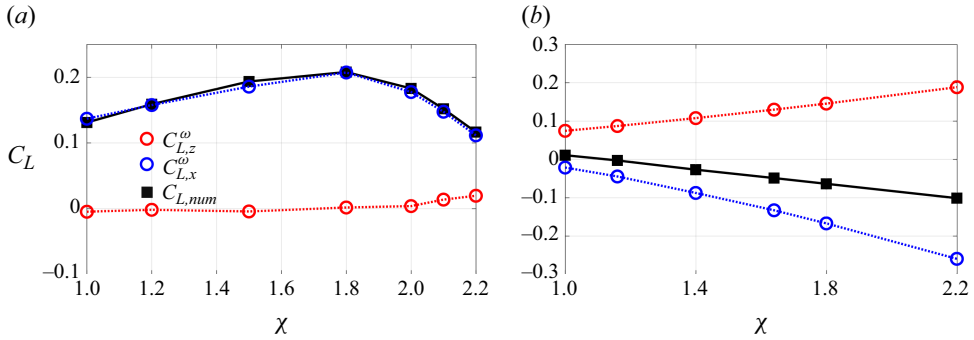


Figure 18. Evolution of the vorticity forces with respect to aspect ratio. (a) Results for bubbles with parameters $(Re, \mu^*) = (300, 0.01)$. (b) Results for rigid spheroids with parameters $(Re, \mu^*) = (50, 100)$.

streamwise vorticities induced by the L -mechanism are the primary contributors to the lift force on the spherical bubble in this Reynolds number range. For rigid spheres, we fix the parameters at $(\mu^*, \chi) = (100, 1.0)$ and vary the Reynolds number in the range of $75 \leq Re \leq 200$. The results, shown in figure 17(b), differ significantly from those of the inviscid bubbles. Specifically, $C_{L,x}^\omega$ remains negative due to the counter-rotating streamwise vortices originating from the S -mechanism or the tilting eddies in the wake. However, $C_{L,num}$ is not necessarily negative, as $C_{L,z}^\omega$ consistently contributes positively, though it decreases with μ^* . These findings suggest that, in the moderate- to high-Reynolds-number regime, the L -mechanism induced streamwise vortices predominantly dictate the lift force on weakly to moderately viscous droplets. In contrast, for moderately to highly viscous droplets, the S -mechanism does not solely determine the lift, but rather, the contribution from the extended Saffman mechanism remains significant.

We also examine the impact of the aspect ratio χ on the interplay between $C_{L,x}^\omega$ and $C_{L,z}^\omega$ in the moderate- to high-Reynolds-number regime. We begin by considering bubbles with parameters $(Re, \mu^*) = (300, 0.01)$, varying the aspect ratio in the range of $1.0 \leq \chi \leq 2.2$. Figure 18(a) shows that $C_{L,x}^\omega$ closely matches $C_{L,num}$ for all aspect ratios studied. The contribution of $C_{L,z}^\omega$ becomes slightly noticeable only at larger aspect ratios ($\chi > 2.0$), due to the azimuthal vorticities scaling with the aspect ratio as $\omega_{\phi,max} \propto \chi^{8/3}$. Thus, for oblate bubbles, the lift induced by streamwise vorticities, whether from the L - or S -mechanism, remains the primary source of the total lift. Conversely, for rigid spheroids with parameters $(Re, \mu^*) = (50, 100)$, figure 18(b) reveals that $C_{L,x}^\omega$ consistently deviates from $C_{L,num}$. The positive values of $C_{L,z}^\omega$ are comparable to the negative values of $C_{L,x}^\omega$, leading to a near-cancellation that results in small negative values for $C_{L,num}$.

In summary, the decomposition of lift using the vorticity moment theory demonstrates that, in the moderate- to high-Reynolds-number regime where either the L - or the S -mechanism may dominate, counter-rotating streamwise vortices are not necessarily the sole or even the primary source of lift in the presence of shear. For droplets with moderate to high viscosity, the asymmetric convection of azimuthal vorticities, termed as the extended Saffman mechanism in the present study, plays a significant role in determining the lift, meaning that the reversal of lift is not synchronised with the reversal of ω_x . However, it remains challenging to quantify the different effects using the vorticity moment method. This is because, when using the momentum of the streamwise vorticity to obtain $F_{L,x}^\omega$, we end up mixing two contributions, one from the S -mechanism and other from the L -mechanism. While we can evaluate which mechanism is dominating based on the sign of $F_{L,x}^\omega$, we are unable to separate the contributions

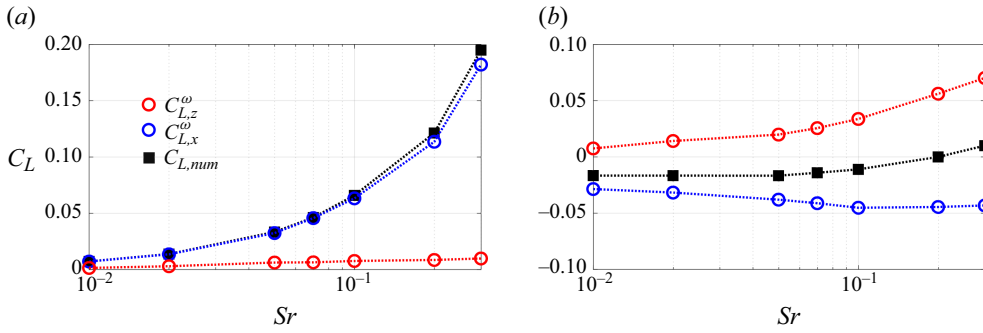


Figure 19. Evolution of the vorticity forces with respect to shear rate. (a) Results for bubbles with parameters $(Re, \mu^*, \chi) = (300, 0.01, 1.0)$. (b) Results for more viscous droplets with parameters $(Re, \mu^*, \chi) = (300, 10, 1.0)$.

from the S - and the L -mechanisms individually. Similarly, the lift force induced by the azimuthal vorticities, which involves both the S - and the extended Saffman mechanisms, cannot be accurately estimated using the current approach. Furthermore, in situations where axisymmetric standing eddies form in the wake of the droplet, the shear flow disrupts their axisymmetric structure, generating counter-rotating streamwise vortices. These tilted eddies also contribute to a negative $F_{L,x}^\omega$, but this contribution cannot be clearly distinguished from the S - or L -mechanisms in the present analysis.

6.2. Influences of the shear rate on the lift

To this point, our analysis has been confined to a constant shear rate of $Sr = 0.2$. However, previous studies on spherical bubbles (Legendre & Magnaudet 1998) and rigid spheres (Kurose & Komori 1999) have demonstrated that the lift force experienced by a body is highly sensitive to variations in the shear rate. Consequently, we will extend our investigation to explore how the lift force evolves with different shear rates on various droplets. Additionally, we will continue to apply the force decomposition method (6.1), based on vorticity moments, to steady problems to elucidate the origin of the lift at these varying shear rates.

We first investigate the effects of shear rate on lift force by analysing bubbles with parameters $(Re, \mu^*, \chi) = (300, 0.01, 1.0)$. The shear rate is varied from 0.01 to 0.3, and the corresponding lift coefficient C_L is depicted in figure 19(a). The data reveal a positive correlation between $C_{L,num}$ and the shear rate Sr . Using (6.1), we decompose the lift into contributions from the streamwise vorticity $C_{L,x}^\omega$ and the azimuthal vorticity $C_{L,z}^\omega$. It is evident that $C_{L,x}^\omega$ closely matches $C_{L,num}$, still indicating that for bubbles, the enhancement in lift is primarily due to the L -mechanism-induced streamwise vortices. For comparison, we consider a more viscous droplet with parameters $(Re, \mu^*, \chi) = (300, 10, 1.0)$ and examine how the lift coefficient changes with shear rate in figure 19(b). As Sr increases, $C_{L,num}$ transitions from negative to positive values, with the transition threshold occurring at $Sr \approx 0.2$. This shift suggests that, at higher shear rates, the contribution from azimuthal vorticities ($C_{L,z}^\omega$) surpasses that from streamwise vorticities ($C_{L,x}^\omega$). Although the negative contribution from $C_{L,x}^\omega$ increases with Sr due to the intensified S -mechanism and more pronounced tilted standing eddies, the positive contribution from $C_{L,z}^\omega$ increases even more sharply, leading to an overall positive lift force. This discrepancy between $C_{L,x}^\omega$ and $C_{L,num}$ underscores that for highly viscous droplets in shear flow, the counter-rotating streamwise vortices in the wake contribute only a portion of the total lift

experienced by the droplet. In addition, we also investigate the influence of the shear rate on unsteady problems characterised by the vortex shedding in the wake of the droplet, and these results are presented and discussed in [Appendix D](#).

In summary, increasing the shear rate (Sr) consistently results in a larger positive lift force on the droplet. This dependency of the lift coefficient C_L on Sr helps explain the discrepancies observed in the Reynolds number (Re) thresholds for lift reversal on a rigid sphere in different studies (Kurose & Komori 1999; Bagchi & Balachandar 2002; Hölzer & Sommerfeld 2009). The mechanisms underlying this lift enhancement vary between weakly to moderately viscous and moderately to highly viscous droplets. For weakly to moderately viscous droplets, a higher Sr enhances the L -mechanism, resulting in increased positive lift. Conversely, for moderately to highly viscous droplets, the lift enhancement is largely attributed to the intensified asymmetric convection of azimuthal vorticities, which is the extended Saffman mechanism that contributes significantly to the positive lift.

7. Conclusions

In this study, we investigate the lateral lift experienced by an oblate droplet translating in a linear shear flow. We employ three-dimensional numerical simulations using a recently developed sharp interface method. This numerical approach allows for droplets of arbitrary shape and viscosity, thus bridging the gap between the well-understood behaviours of inviscid bubbles and rigid spheres in shear flow. Our primary goal is to explore the effects of various parameters on the lateral lift over a broad parameter space defined by Reynolds number (Re_e), viscosity ratio (μ^*) and aspect ratio (χ). The Reynolds number ratio (Re^*) and shear rate (Sr) are considered secondary aspects in our investigation.

In the low-but-finite Re regime, our numerical results confirm the validity of the analytical solution derived by Legendre & Magnaudet (1997) for the lift force on a spherical droplet of arbitrary viscosity. Specifically, the lift force is proportional to the square of the drag experienced by the droplet, which can be expressed as $F_L \propto \mathcal{R}^2 = [(3\mu^* + 2)/(\mu^* + 1)]^2$. Consequently, the ratio of the forces experienced by an inviscid bubble and a solid sphere is $(2/3)^2$. This is known as the Saffman mechanism, which arises due to the asymmetric advection of the vorticity produced at the droplet's interface in the low but non-vanishing Re regime. For an ellipsoidal droplet, we find that increased oblateness enhances the positive lift because it increases the curvature of the interface, leading to more vorticity production. We propose a general semi-empirical solution to normalise the lift experienced by droplets ranging from spheres to spheroids, and our correlation aligns well with the numerical results.

In the moderate- to high- Re regime, our numerical findings reveal that for a spherical droplet, increasing the viscosity ratio μ^* causes a reduction in the positive lift force, and a reversal to small negative values is observed beyond a certain threshold of μ^* . This finding bridges the gap between previous studies on spherical bubbles and rigid spheres, providing insight into how the lift transitions from positive values in bubbles to negative values in rigid spheres. Our results show that for weakly to moderately viscous droplets, the L -mechanism predominates. In this scenario, the shear-contained vorticity is stretched and tilted by the droplet, generating streamwise vorticities that contribute to a positive lift force. As μ^* increases, attached eddies form at the droplet's rear and the shear flow tilts these eddies, leading to streamwise vortices that produce a negative lift force – an effect we refer to as the S -mechanism. Notably, the sign reversal of the lift force lags behind the sign reversal of the streamwise vorticities. For oblate droplets in this regime, the L -mechanism becomes increasingly significant for moderately deformed droplets and we observe that

the lift coefficient C_L increases with the aspect ratio χ up to an Re -dependent critical aspect ratio, χ_{cr} , for weakly to moderately viscous droplets. For highly deformed droplets ($\chi > \chi_{cr}$) or moderately to highly viscous droplets, the S -mechanism prevails, leading to a decrease or even reversal of the lift force. However, the sign reversal of the lift force does not synchronise with the sign reversal of the streamwise vorticities. This phase difference suggests that an additional mechanism, likely related to the asymmetric advection of azimuthal vorticities at the droplet's interface, plays a significant role in offsetting part of the negative lift induced by the S -mechanism.

Our study has elucidated how the counter-rotating streamwise vorticities, induced by the L - and S -mechanisms, interact to influence the lift force on droplets in shear flow. Given that these vorticities exhibit opposite signs, a natural approach is to compare the total lift with the lift induced specifically by streamwise vorticities. Using the theory of vorticity moments, we decompose the lift force into components arising from the z -component azimuthal vorticity and the x -component streamwise vorticity. Our decomposition results indicate that, in the moderate- to high-Reynolds-number (Re) regime, the lift induced by ω_x closely approximates the total lift for weakly to moderately viscous droplets. This finding suggests that the L -mechanism predominantly governs the lift generation in this regime. Conversely, for moderately to highly viscous droplets, the ω_x -induced lift only accounts for a portion of the total lift, with this proportion being highly dependent on the parameters (Re , μ^* , χ). The results demonstrate that the S -mechanism alone cannot solely determine the magnitude or direction of the lift in shear flow. This is due to the fact that the asymmetric advection of azimuthal vorticities can generate a positive lift, in terms of the extended Saffman mechanism, that offsets part of the negative lift produced by the S -mechanism. Under certain conditions, this positive contribution from azimuthal vorticities can even dominate. Further analysis based on the same theory of vorticity moments shows that the dominance of the L - and S -mechanisms in producing lift varies with different shear rates. This underscores that the mechanisms governing lift in shear flow are complex and depend on multiple factors, including viscosity, aspect ratio and shear rate.

In summary, our study clarifies the effects of droplet viscosity and aspect ratio on lift forces in linear shear flow and confirms the origins of lift in various flow regimes. However, there are opportunities for more systematic investigations in the future. For example, exploring the impact of the Reynolds number ratio between the interior and exterior flows of the droplet could provide further insights. We observed that ([Appendix E](#)) when Re^* exceeds a certain threshold, secondary instabilities can be triggered within the droplet's flow. Additionally, the A -mechanism – referring to the asymmetric deformation of the droplet – merits further attention, particularly in the low- to moderate- Re regime.

Acknowledgements. The authors thank Professor Jacques Magnaudet and Dr. Pengu Shi for their insightful discussions on the Saffman mechanisms, which greatly enhanced our understanding of this aspect. We also appreciate the anonymous reviewers for their constructive comments, which have substantially improved the quality of the paper.

Funding. The authors gratefully acknowledge the support from National Key R & D Program of China (grant nos 2023YFA1011000, 2022YFE03130000) and from the NSFC (grant nos 12222208, 11988102).

Declaration of interests. The authors report no conflict of interest.

Appendix A. Numerical methods and validations

This appendix presents a description and validation of the numerical methods we developed for simulating shear flow past a viscous droplet, accounting for both internal

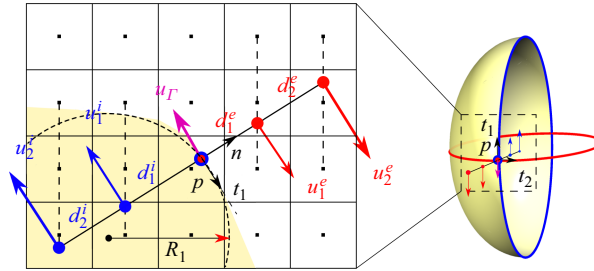


Figure 20. Sketch of the embedded boundary method used to estimate the interfacial velocity in the t_1 direction, given $u_{\tau_1}|_{\Gamma}$. This figure corresponds to (A1). The shaded region represents the flow field inside the droplet, while the blank region is the flow field outside the droplet.

and external flows. As introduced in § 3, the method is incorporated into the open-source library *Basilisk*, which solves the Navier–Stokes equations with second-order accuracy. In this section, we focus on the treatment of the interfacial boundary conditions (3.1) featuring our implemented algorithms. More detailed information can be found in our companion paper (Wei *et al.* 2023).

A.1 Key techniques of numerical methods

Focusing on (3.1), the main difficulty in using Cartesian grids is obtaining the normal derivative of the tangential velocity components at the interface, $(\frac{\partial u_{k,\tau_{1,2}}}{\partial n})|_{\Gamma}$. This challenge arises because the mesh boundaries do not align with the droplet interface. The interface is reconstructed by piecewise linear segments that divide the interfacial meshes into two parts. In this scenario, the estimation of tangential velocities $u_{\tau_{1,2}}|_{\Gamma}$ relies on the local body-fitted system comprising $(\mathbf{n}, \mathbf{t}_1, \mathbf{t}_2)$. To address this problem, we develop two key techniques.

The first technique is an embedded boundary method, which estimates the tangential components of interfacial velocities, i.e. $u_{\tau_{1,2}}|_{\Gamma} = \mathbf{u}(x, y, z) \cdot \mathbf{t}_{1,2}|_{\Gamma}$. These components must satisfy the jump conditions described by (3.1b) and (3.1c). Figure 20 illustrates how to calculate $u_{\tau_1}|_{\Gamma}$ along the tangent direction \mathbf{t}_1 at point P . The jump condition (3.1b) leads to the following formulation:

$$u_{\tau_1}|_{\Gamma} = \left[\frac{1}{R_1} + \frac{d_1^e + d_2^e}{d_1^e d_2^e} + \mu^* \left(\frac{d_1^i + d_2^i}{d_1^i d_2^i} - \frac{1}{R_1} \right) \right]^{-1} \left(\frac{d_2^e}{d_1^e (d_2^e - d_1^e)} u_1^e - \frac{d_1^e}{d_2^e (d_2^e - d_1^e)} u_2^e + \mu^* \frac{d_2^i}{d_1^i (d_2^i - d_1^i)} u_1^i - \mu^* \frac{d_1^i}{d_2^i (d_2^i - d_1^i)} u_2^i \right). \quad (\text{A1})$$

Here, $u_{1,2}^{i,e}$ are the velocities at the intersection points parallel to \mathbf{t}_1 , belonging to the local body-fitted system, $d_{1,2}^{i,e}$ are the corresponding distances from the interface and R_1 is the local curvature radius of point P corresponding to τ_1 . Equation (A1) is a second-order accurate interpolation scheme, indicating that the interfacial velocity depends on both the internal and external flow. Similarly, $u_{\tau_2}|_{\Gamma}$ can be estimated via a similar interpolation scheme, where the curvature radius is now R_2 .

The next step is to transform the obtained tangential velocities $(u_{\tau_{1,2}})|_{\Gamma}$ and $(u_n)|_{\Gamma} = 0$ into the Cartesian system, given $(\mathbf{u}(x, y, z))|_{\Gamma}$, which are required for the solution of the Navier–Stokes equations (2.1). In the present numerical method, we solve the fluid flow inside and outside the droplet separately by imposing $(\mathbf{u}(x, y, z))|_{\Gamma}$ as interfacial

conditions. The mapping of these velocities between the two systems relies heavily on the estimated directions $\mathbf{t}_{1,2}$ and values $R_{1,2}$. This is the second technique developed in our numerical method.

Without loss of generality, we return to spatial analytic geometry (Kühnel 2015), assuming the parametric surface of the interface is expressed as $\Gamma : \mathbf{p}(\eta, \xi)$, where (η, ξ) parametrise the surface. The curvature formulae rely on the associated first and second fundamental forms, denoted by $\mathbb{I}(\eta, \xi)$ and $\mathbb{III}(\eta, \xi)$, respectively, which have the following form:

$$\mathbb{I} = \begin{bmatrix} \mathbf{p}_\eta \cdot \mathbf{p}_\eta & \mathbf{p}_\eta \cdot \mathbf{p}_\xi \\ \mathbf{p}_\xi \cdot \mathbf{p}_\eta & \mathbf{p}_\xi \cdot \mathbf{p}_\xi \end{bmatrix}, \quad \mathbb{III} = \begin{bmatrix} \mathbf{p}_{\eta\eta} \cdot \mathbf{n} & \mathbf{p}_{\eta\xi} \cdot \mathbf{n} \\ \mathbf{p}_{\xi\eta} \cdot \mathbf{n} & \mathbf{p}_{\xi\xi} \cdot \mathbf{n} \end{bmatrix} = - \begin{bmatrix} \mathbf{p}_\eta \cdot \mathbf{n}_\eta & \mathbf{p}_\eta \cdot \mathbf{n}_\xi \\ \mathbf{p}_\xi \cdot \mathbf{n}_\eta & \mathbf{p}_\xi \cdot \mathbf{n}_\xi \end{bmatrix}, \quad (\text{A2})$$

where $\mathbf{p}_\eta = \partial\mathbf{p}/\partial\eta$, $\mathbf{p}_\xi = \partial\mathbf{p}/\partial\xi$ and $\mathbf{p}_{\eta\eta} = \partial\mathbf{p}_\eta/\partial\eta$, $\mathbf{p}_{\eta\xi} = \partial\mathbf{p}_\eta/\partial\xi$, $\mathbf{p}_{\xi\xi} = \partial\mathbf{p}_\xi/\partial\xi$ denote the first and second partial derivatives, respectively. Then, the principal directions and principal curvatures $\kappa_{1,2}$ can be obtained through the eigenvector $\mathbf{c}(\eta, \xi)$ and eigenvalue λ of the Weingarten matrix $\mathbb{W} = [\mathbb{III}][\mathbb{I}^{-1}]$ by

$$\mathbb{W}\mathbf{c} = \lambda\mathbf{c}. \quad (\text{A3})$$

Here, the principal curvatures $\kappa_1 = \lambda_1$ and $\kappa_2 = \lambda_2$ are used to estimate $R_1 = 1/\kappa_1$ and $R_2 = 1/\kappa_2$ as shown in (A1). Correspondingly, the principal directions of (η, ξ) or $(\mathbf{t}_1, \mathbf{t}_2)$ can be derived as $\mathbf{t}_1 = (\mathbf{p}_\eta, \mathbf{p}_\xi)\mathbf{c}_1$, $\mathbf{t}_2 = (\mathbf{p}_\eta, \mathbf{p}_\xi)\mathbf{c}_2$.

The numerical solution of (A3) depends heavily on evaluating \mathbb{I} and \mathbb{III} , which require calculating the derivatives of \mathbf{p} . If the interface is given explicitly, such as a spherical or ellipsoidal shape, these derivatives can be determined analytically (Kempe *et al.* 2015). However, for droplets with arbitrary shapes, estimating these derivatives is challenging. We propose a height function-based approach to estimate the derivatives of \mathbf{p} . This involves using coupled level-set and volume-of-fluid methods to determine the height functions (h) and their derivatives in the interfacial grids, resulting in

$$\mathbb{I} = \begin{bmatrix} 1 + h_x^2 & h_x h_y \\ h_y h_x & 1 + h_x^2 \end{bmatrix} \quad \mathbb{III} = \begin{bmatrix} n_z h_{xx} & n_z h_{xy} \\ n_z h_{yx} & n_z h_{yy} \end{bmatrix} \quad n_z \geq n_y \geq n_x, \quad (\text{A4})$$

where the estimation of h is detailed in § (3.2) by Wei *et al.* (2023), while n is the normal direction, $h_{x,y}$ and $h_{xx,yy,xy}$ are the first and second partial derivatives, respectively. After obtaining \mathbb{I} and \mathbb{III} in (A4), (A3) can be solved, providing the corresponding principal vectors $(\mathbf{t}_1, \mathbf{t}_2)$ and principal curvature radii (R_1, R_2) . After that, the interfacial velocity $(u_{\tau_{1,2}})|_\Gamma$ in the local body-fitted system as well as $(\mathbf{u}(x, y, z))|_\Gamma$ in the Cartesian system can be obtained via (A1), then the remaining step is to solve the velocity–pressure coupling equations in the framework of the embedded boundary method, which enables the flow fields to be solved separately in the exterior and the exterior of the droplet.

A.2 Validations of numerical methods

Sections 4 and 5 have already demonstrated that our numerical results compare well with benchmark solutions, as shown in figures 3, 9 and 11. These figures highlight the excellent agreement observed across the low- to moderately high-Reynolds-number (Re) regime. This appendix provides additional validation tests, including grid and domain size independence studies, as well as proof of numerical accuracy.

The first validation test examines grid independence in our simulations. For this, we considered a rigid sphere with parameters $(Re, \mu^*, \chi, Sr) = (200, 100, 1.0, 0.2)$, which corresponds to a boundary layer thickness of $\delta \approx R/7$. For comparison, the numerical result reported by Kurose & Komori (1999) is also included. Figure 21(a) shows the time evolution of the lift coefficient C_L as the grid size surrounding the droplet is

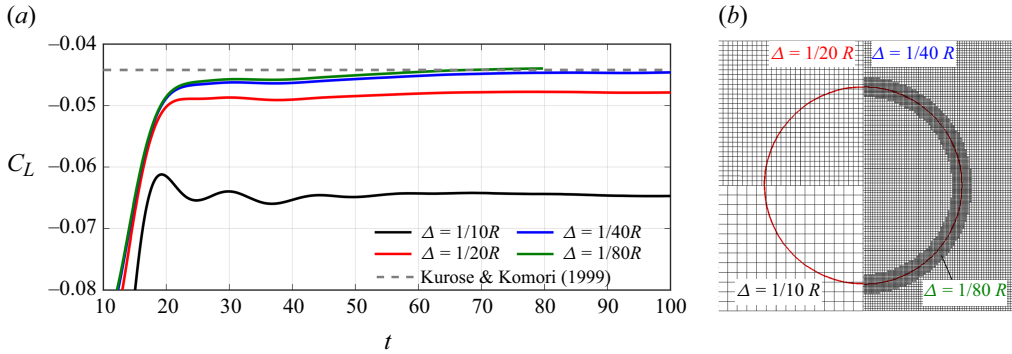


Figure 21. Grid independence test results for a droplet with parameters $(Re, \mu^*, \chi, Sr) = (200, 100, 1.0, 0.2)$. (a) Time evolution of the lift coefficient C_L as a function of grid size, while the numerical result reported by Kurose & Komori (1999) is also included. (b) Mesh distributions around the droplet for different spatial resolutions.

Domain size (L)	50R	100R	200R	400R	800R	Reference
$C_L (Re = 0.1)$	0.926	1.525	1.987	2.239	2.249	2.2406
$C_L (Re = 200)$	0.1289	0.1266	0.1264	0.1263	0.1263	0.1258

decreased from $\Delta = R/10$ to $\Delta = R/80$. The results indicate that as the mesh is refined, C_L converges to approximately -0.44 , closely matching the result from Kurose & Komori (1999). Figure 21(b) displays the mesh distributions around the droplet at different spatial resolutions. Based on this convergence study, a spatial resolution of $\Delta = R/80$ is used throughout the present study.

A second series of tests was conducted to determine the optimal size L of the computational domain. Simulations were performed for six domains extending up to $L = 50R, 100R, 200R, 400R$ and $800R$. These tests were conducted on bubbles ($\mu^* = 0.01$) at both low ($Re = 0.1$) and high Reynolds numbers ($Re = 200$) for a non-dimensional shear rate $Sr = 0.2$. The lift coefficients obtained from these simulations are reported in table 1, with reference data provided by the correlations in (4.1),(4.2a) and (5.1) (Legendre & Magnaudet 1998), respectively. At high Reynolds numbers, a domain extending up to $50R$ is sufficient, as no significant changes are observed in the drag or lift forces when the domain size is increased. However, for low Reynolds numbers, confinement effects significantly influence the lift force. A domain extending up to $400R$ is necessary to capture all the inertial effects contributing to the lift accurately. Based on these tests, the computational domain for most simulations is set to $L = 200R$ for $Re > 1$, while it is increased to $L = 400R$ for $Re \leq 1$.

A third series of tests was conducted to verify the accuracy of the numerical algorithm. While figure 21 and table 1 demonstrate validity in simulating shear flow past a rigid sphere and an inviscid bubble, we further tested flow past oblate bubbles and spherical droplets to investigate the influences of the aspect ratio and viscosity ratio, respectively. For an oblate bubble with an aspect ratio of $\chi = 1.5$, figure 22(a) shows the dimensionless value of $\chi C_L / (Sr C_D)$ against various Re . Numerical and analytical solutions provided

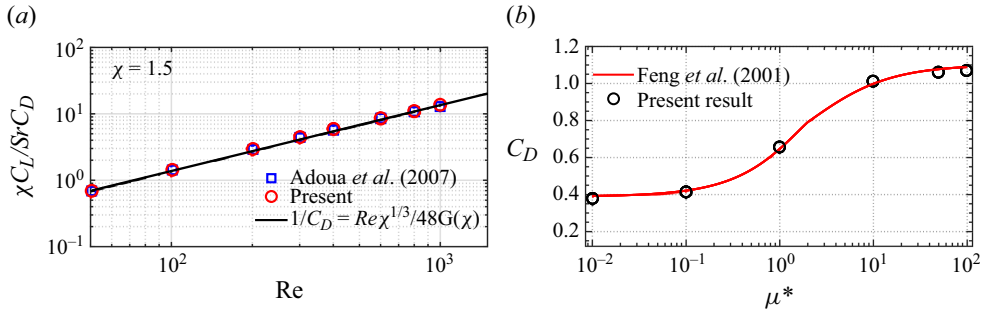


Figure 22. (a) Dimensionless parameter $\chi C_L / (Sr C_D)$ for an oblate bubble with $\chi = 1.5$ across various Reynolds numbers. (b) Drag coefficients for spherical droplets at $Re = 100$ and $Sr = 0.2$ with varying viscosity ratios μ^* . In panel (a), the numerical and analytical solutions are provided by Adoua (2007); and in panel (b), the semi-analytical correlation is established by Feng & Michaelides (2001) for homogeneous flow past a spherical droplet.

Reference	Domain size (L/R)	Sr	Numerical method	C_L
Kurose & Komori (1999)	10	0.2	Marker-and-cell method	-0.016
Bagchi & Balachandar (2002)	30	0.2	Fourier-Chebyshe scheme	-0.015
Hölzer & Sommerfeld (2009)	12.4	0.04	Lattice Boltzmann method	-0.01
Homann et al. (2013)	256	0.2	Pseudo-Fourier-spectral method	-0.002
Kim (2006)	100	0.1	Alternating-direction-implicit method	-0.008
Lee & Wilczak (2000)	16	0.2	Finite element method	-0.012
Present study	200	0.2	Cartesian grid technique	-0.008

Table 2. Reported lift coefficients for a rigid particle translating in the shear flow at $Re = 100$.

by Adoua (2007) are used for comparison. Our results show excellent agreement with reference data across a wide range of Reynolds numbers, from $Re = 50$ to $Re = 1000$. For the case of shear flow past spherical droplets, simulations were performed at $Re = 100$ and $Sr = 0.2$, with viscosity ratios varying from $\mu^* = 0.01$ to $\mu^* = 100$. The drag coefficients are presented in figure 22(b), alongside the semi-analytical correlation established by Feng & Michaelides (2001) for homogeneous flow past a spherical droplet (see (36), (37) in their paper). Once again, our numerical results show good consistency with the correlation, indicating that such moderate shear rates have negligible influence on drag, as also identified by previous studies (Legendre & Magnaudet 1998; Bagchi & Balachandar 2002; Adoua et al. 2009). The results presented in figure 22 confirm the accuracy and reliability of our numerical method, particularly its capability to solve viscous flow past oblate droplets.

Appendix B. Lift coefficient for a rigid particle of $Re = 100$ in different numerical studies

The transition Reynolds number (Re) for the sign reversal of the lift force on a rigid sphere is known to vary across different numerical studies, as reviewed by Shi & Rzehak (2019). This discrepancy arises due to differences in numerical settings, including computational domain size, boundary conditions and grid resolution. In this appendix, we further review the lift force experienced by a rigid sphere at a fixed Reynolds number of $Re = 100$, with results summarised in table 2. The table also outlines the numerical methods used in the

respective studies. Interestingly, the reported lift coefficients (C_L) show notable variability, with Homann *et al.* (2013) accounting for the rotation of the sphere in their analysis. Their findings highlight that the computational domain size significantly affects C_L in this Reynolds number regime, likely because the lift coefficient is relatively small and hence more sensitive to numerical details. For example, Homann *et al.* (2013) observed a decreasing trend in C_L as the computational domain size was increased from $256R$ to $512R$, emphasising the importance of domain size in accurately capturing the lift force. This observation suggests that future numerical studies should rigorously quantify the influence of computational domain size and boundary conditions on C_L , particularly near the transition Reynolds number. Such studies would provide deeper insights into the sensitivity of lift force predictions and improve the reliability of numerical simulations in this regime.

Appendix C. Force decomposition by using vorticity moment

C.1 Force estimation formula

Vorticity moments can be applied to estimate the total force \mathbf{F} acting on a body translating steadily in a viscous fluid. Still using figure 15(b) for illustration, the force is given by the following formulation (Wu *et al.* 2007b):

$$\mathbf{F} = -\frac{d}{dt} \left(\frac{1}{2} \int_{\Omega_i + \Omega_e} \mathbf{r} \times \boldsymbol{\omega} d\Omega \right) + \rho \int_{S_e} \mathbb{T} \cdot \mathbf{n} dS, \quad (\text{C1})$$

where Ω_i is the internal volume occupied by the body, Ω_e is the volume of the liquid surrounding the body, S_e is the external boundary of the domain Ω_e and \mathbf{n} is the outward unit normal vector of S_e . Here, \mathbb{T} is a second-order tensor, defined as

$$\begin{aligned} \mathbb{T} = & -\frac{1}{2} \mathbf{u}'(\mathbf{r} \times \boldsymbol{\omega}) + \frac{1}{2} |\mathbf{u}'|^2 \mathbb{I} - \mathbf{u}' \mathbf{u}' + \frac{1}{2} \boldsymbol{\omega}(\mathbf{r} \times \mathbf{u}') \\ & + \frac{1}{2} \nu \left[(\mathbf{r} \cdot \nabla^2 \mathbf{u}') \mathbb{I} - \mathbf{r} \nabla^2 \mathbf{u}' \right] + 2\nu \mathbb{S}', \end{aligned} \quad (\text{C2})$$

with \mathbf{u}' is the velocity disturbance field induced by the presence of the moving object. Note that (C1) is derived from the full Navier–Stokes equations where the only assumption is that the object moves steadily. Then, the viscous contribution appears explicitly in the surface integral over S_e . However, thanks to the decaying property of $|\mathbf{u}'| \sim r^{-3}$ (with $r = |\mathbf{r}|$) in a high- Re flow characterised by the moving velocity of the object, we would expect all terms appearing in (C2) to vanish if the integral boundary of the selected domain is far from the body, provided that S_e contains all the flow disturbance. In contrast, for low-Reynolds-number flows, omitting the contributions from S_e is infeasible. In this regime, $|\mathbf{u}'|$ scales as r^{-1} and the viscosity-related terms in \mathbb{T} scale as νr^{-2} . As a result, the surface integral over S_e does not necessarily converge when the domain size approaches infinity. Therefore, estimating \mathbf{F} in this limit requires accounting for the contribution from S_e , which is rather tedious. For the moderate- to high- Re cases considered in the manuscript, with $Re > 50$, if we select S_e to be sufficiently far away from the moving object, (C1) can be simplified to the following formula (Saffman 1995):

$$\mathbf{F} = -\frac{d}{dt} \left(\frac{1}{2} \int_{\Omega_i + \Omega_e} \mathbf{r} \times \boldsymbol{\omega} d\Omega \right). \quad (\text{C3})$$

The x -component of the force refers to the drag, while the y -component is the lift, which is the primary focus of this study. The lift force, F_y or F_L , can be further expressed as

$$F_L = -\frac{d}{dt} \left(\frac{1}{2} \int_{\Omega_i + \Omega_l} (\omega_z x - \omega_x z) d\Omega \right). \quad (C4)$$

Equation (C4) can be decomposed into two contributions, from the azimuthal vorticity (ω_z on the XOY plane) and the streamwise vorticity respectively

$$F_{L,z}^\omega = -\frac{d}{dt} \left(\frac{1}{2} \int_{\Omega_i + \Omega_l} \omega_z x d\Omega \right), \quad F_{L,x}^\omega = \frac{d}{dt} \left(\frac{1}{2} \int_{\Omega_i + \Omega_l} \omega_x z d\Omega \right). \quad (C5)$$

Equation (C5) provides a clear method for estimating the lift forces arising from different components of the vorticity moment. Then, these contributions can be further approximated as follows:

$$F_{L,z}^\omega = -\frac{1}{2} \left(\rho_l U \int_{\Omega_i + \Omega_e} \omega_z d\Omega + \int_{S_e} \omega_z x \mathbf{u} \cdot \mathbf{n} dS_e \right),$$

$$F_{L,x}^\omega = \frac{1}{2} \rho_l U \int_{A_{wake}} \omega_x z dA. \quad (C6)$$

These expressions correspond to (6.1) and offer a detailed breakdown of the lift force into its constituent vorticity components, providing deeper insights into the flow dynamics involved. However, still note that due to the approximation we made from (C1) to (C3), the vorticity induced lift estimated from (6.1) (or (C6)) may have a slight discrepancy from the numerical value provided by (2.4).

C.2 l_A and r_A independence study

As discussed in the calculation of the streamwise vorticity-induced lift force (see figure 15b), it is crucial to select appropriate values of l_A and r_A , which define the selection of A_{wake} used in the integration formula (6.1). This is essentially ascribed to two reasons: one is because the values of $\int_{S_e} \mathbb{T} \cdot \mathbf{n} dS_e$ appearing in (C1) cannot fully vanish if l_A is not far enough and the other is due to the fact that A_{wake} cannot contain all the streamwise vorticities if r_A is not large enough. Therefore, independence studies of l_A and r_A were conducted through two series of tests. The first tests are the same as those presented in figure 15, with constant parameters $(Re, \chi, Sr) = (100, 1.0, 0.2)$ and varying viscosity ratios $0.01 \leq \mu^* \leq 100$. Before presenting the results of the tests, it is important to note that during this post-processing phase, the grid size of $\Delta = R/20$ was expanded to cover a broader range of $(x, z) \in ([-5R, 16R], [-7R, 7R])$, compared with the simulation range of $(x, z) \in ([-2R, 5R], [-2R, 2R])$. This adjustment was made to capture the vorticity magnitude with greater precision, thereby ensuring that the effects of l_A and r_A on the computed lift force were accurately assessed.

Figure 23 shows how $\overline{C}_{L,\omega_x}$ varies with different values of l_A and r_A . Here, $\overline{C}_{L,x}^\omega$ is the value of $C_{L,x}^\omega$ normalised by that at $(l_A, r_A) = (16R, 4.6R)$ to enhance readability. The results converge to 1 as l_A and r_A increase, indicating that the chosen values of $(l_A, r_A) = (14R, 4.4R)$ for surface integration are sufficient to obtain converging results. Additionally, a series of numerical tests were performed on an inviscid bubble with parameters $(Re, \mu^*, \chi) = (300, 0.01, 1.0)$, with the shear rate varying in the range of $0.01 \leq Sr \leq 0.3$. These tests are also presented in figure 19(a). The l_A and r_A independence study, shown in figure 24, confirms that $(l_A, r_A) = (14R, 4.4R)$ is sufficient to ensure convergence in $C_{L,x}^\omega$. Then, $(l_A, r_A) = (14R, 4.4R)$ are chosen throughout the present study.

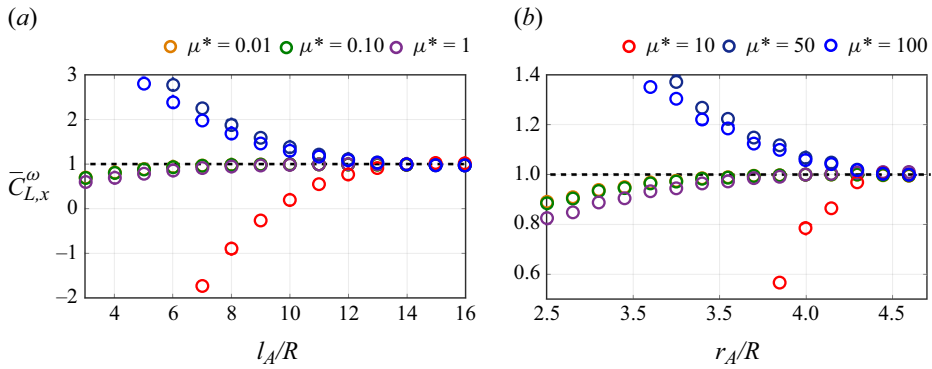


Figure 23. Normalised values of $\bar{C}_{L,x}^{\omega}$ for varying l_A and r_A , with constant parameters $(Re, \chi, Sr) = (100, 1.0, 0.2)$. The results show convergence towards 1 as l_A and r_A increase to $(l_A, r_A) = (14R, 4.4R)$. $\bar{C}_{L,x}^{\omega}$ is the value of $C_{L,x}^{\omega}$ normalised by that at $(l_A, r_A) = (16R, 4.6R)$.

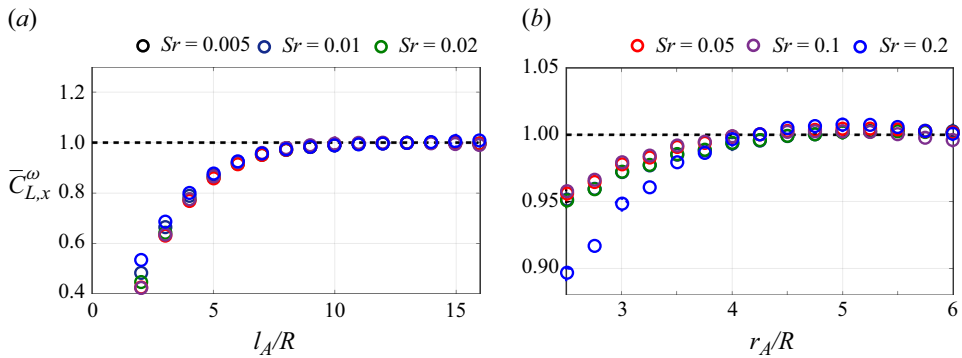


Figure 24. Independence study of l_A and r_A for $\bar{C}_{L,x}^{\omega}$ showing sufficient convergence at $(l_A, r_A) = (14R, 4.4R)$.

Appendix D. Influences of the shear rate on the lift force for unsteady problems

We also investigate how the shear rate influences the lift force in an unsteady problem, which is characterised by vortex shedding in the wake of the droplet. Initially, we analyse a rigid sphere with parameters $(Re, \mu^*, \chi) = (300, 100, 1.0)$. The effect of shear rate on lift forces is illustrated in figure 25(a), which shows only the oscillatory period. At low to moderate shear rates ($0 \leq Sr \leq 0.2$), we observe persistent unsteady oscillations, with only minor changes in oscillatory frequency and amplitude. For instance, $C_L(Re = 300, \mu^* = 100, \chi = 1.0, Sr \leq 0.02) \approx C_{L,bi}(Re = 300, \mu^* = 100, \chi = 1.0, Sr = 0)$. Quantitative analysis using fast Fourier transform reveals a slight increase in the dominant oscillatory frequency with Sr , as shown in figure 25(b). This result is consistent with findings by Sakamoto & Haniu (1995) and Kurose & Komori (1999), who first reported and confirmed the effect of shear rate on the oscillatory frequency in rigid spheres. At $Sr = 0.5$, the flow becomes nearly steady, though the lift force remains negative. Beyond $Sr = 0.5$, numerical instabilities arise at $Re = 300$ on a rigid sphere, preventing further computation of the lift force. However, as indicated by figure 19(b), the lift may revert to positive values if Sr is sufficiently large. Figure 25(c) illustrates the iso-surfaces of $\omega_x = \pm 0.3$, showing how vortices transition from unsteady shedding to a steady counter-rotating structure with increasing Sr .

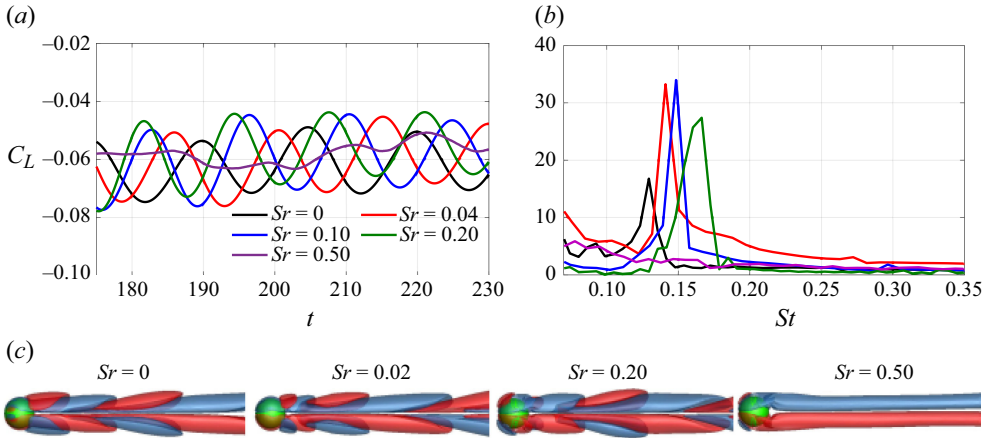


Figure 25. Influences of shear rate on the unsteady behaviours of a rigid sphere with parameters $(Re, \mu^*, \chi) = (300, 100, 1.0)$. (a) Time histories of the lift coefficient C_L versus shear rate Sr . (b) Fast Fourier transform analysis of the curves shown in panel (a). (c) Iso-surfaces of $\omega_x = \pm 0.3$ for different shear rates.

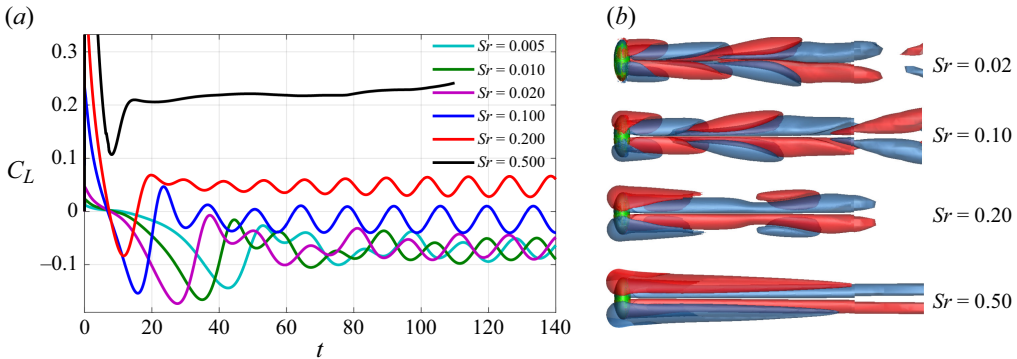


Figure 26. Influences of shear rate on the unsteady behaviours of an oblate bubble with parameters $(Re, \mu^*, \chi) = (300, 0.01, 2.5)$. (a) Time histories of the lift coefficient C_L versus shear rate Sr . (b) Iso-surfaces of $\omega_x = \pm 0.3$ for various shear rates.

Next, we investigate the impact of shear rate on an oblate bubble with parameters $(Re, \mu^*, \chi) = (300, 0.01, 2.5)$. Figure 26(a) presents the time evolution of C_L for various Sr values. For small to moderate shear rates ($0.005 \leq Sr \leq 0.2$), the droplet exhibits unsteady behaviour, with C_L transitioning from negative to positive values. This observation suggests that higher shear rates not only suppress vortex shedding but also enhance the L -mechanism, leading to a reversal in the lift direction. Furthermore, increasing the shear rate further raises the positive value of C_L from 0.05 at $Sr = 0.2$ to 0.22 at $Sr = 0.5$. Figure 26(b) shows the iso-surfaces of $\omega_x = \pm 0.3$ for different shear rates. Shear rates below $Sr \leq 0.1$ exhibit periodic shedding, while $Sr \geq 0.2$ reveals two pairs of counter-rotating vortex structures respectively corresponding to the S - and L -mechanisms, similar to those discussed in figure 14. These vortex structures further support the conclusion that increasing Sr enhances the L -mechanism in weakly to moderately viscous droplets.

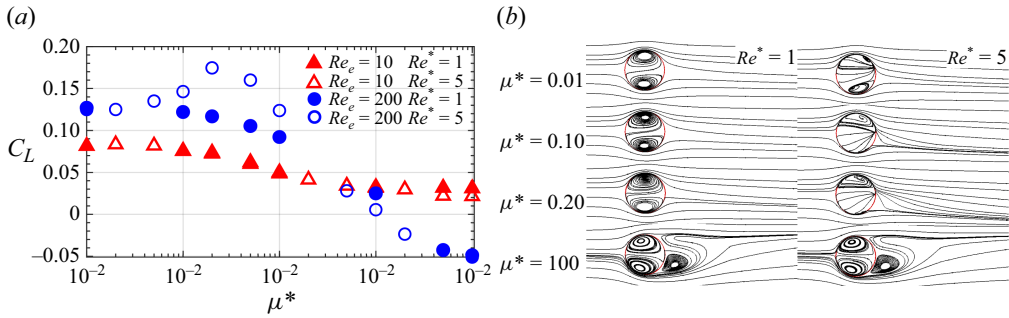


Figure 27. Lift coefficients for droplets with varying Reynolds number ratios ($Re^* = 1$ and $Re^* = 5$) at different external Reynolds numbers: $Re_e = 10$ and $Re_e = 200$. (a) Variation of C_L against μ^* . (b) Velocity streamlines on XOY plane at different viscosity ratios and Reynolds number ratios, while the external Reynolds number is maintained at $Re_e = 200$.

Appendix E. Influences of the Reynolds number ratio on the lift

Throughout this study, we have maintained the Reynolds number ratio at a constant value of $Re^* = 1$. In this section, we explore the influence of the Reynolds number ratio, Re^* , on lift forces. The Reynolds number for a given fluid is defined as $Re_k = \rho_k U D / \mu_k$, where the variation of Re^* in this study is achieved by adjusting the density ratio $\rho^* = \rho_i / \rho_e$, as μ^* may vary across cases. We focus on two groups of droplets characterised by $(Re_e, \chi, Sr) = (10, 1.0, 0.2)$ and $(Re_e, \chi, Sr) = (200, 1.0, 0.2)$, with a viscosity ratio in the range of $0.01 \leq \mu^* \leq 100$. Figure 27(a) shows the lift coefficients experienced by droplets with Reynolds number ratios of $Re^* = 1$ and $Re^* = 5$. For droplets at $Re_e = 10$, the lift coefficients as a function of μ^* are nearly independent of Re^* . In contrast, for droplets at $Re_e = 200$, an abnormal increase in C_L is observed in the regime $0.05 \leq \mu^* \leq 10$ when comparing $Re^* = 5$ and $Re^* = 1$, while C_L remains almost the same outside this regime.

These results strongly indicate that for moderately high Reynolds numbers ($Re_e = 200$), increasing the internal Reynolds number of the droplet can lead to flow bifurcation. This phenomenon was also reported by Edelmann *et al.* (2017) for droplets translating in a homogeneous flow, where at low Re_i , the internal flow field resembled the well-known Hill's vortex solution, while higher Re_i led to quasi-steady internal circulation. Additionally, Edelmann *et al.* (2017) identified that flow bifurcation affected drag only when μ^* was within a moderate range, consistent with our observations in figure 27(a). However, they did not explore the lateral forces acting on the droplet in shear flow during internal flow bifurcation. For droplets at $Re_e = 200$, figure 27(b) compares the flow fields in the XOY plane for $Re^* = 1$ (top panel) and $Re^* = 5$ (bottom panel). Evidently, for an inviscid bubble ($\mu^* = 0.01$) and a rigid sphere ($\mu^* = 100$), the external flow fields are nearly identical between the two Re^* , resulting in the same values of C_L . However, for moderately viscous droplets ($\mu^* = 0.1$ and 0.2), internal flow bifurcation occurs, leading to a more unstable external flow, which manifests as an increase in the lift acting on the droplet.

Furthermore, we maintained droplet parameters at $(Re_e, \mu^*, \chi, Sr) = (200, 0.2, 1.0, 0.2)$ and varied the Reynolds number ratio in the range of $0.5 \leq Re^* \leq 5$. Figure 28(a) displays the time histories of the lift coefficients. We observe that at $Re^* = 0.5$ and 1 , the lift coefficients are nearly equal, with $C_L \simeq 0.12$, indicating similar internal flow patterns. At $Re^* = 2$, a slight increase in C_L is observed around $t \simeq 50$, indicating the onset of flow bifurcation. At $Re^* = 5$, the lift coefficient increases sharply at $t \simeq 30$ and eventually stabilises at $C_L \simeq 0.18$, with slight oscillations. These results

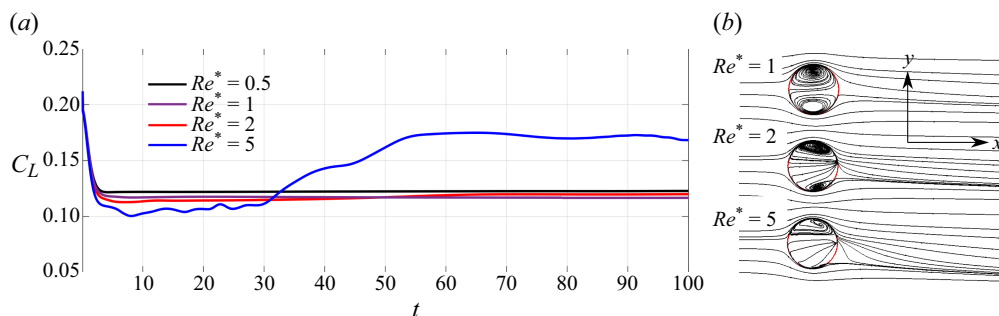


Figure 28. Lift variations for droplets with varying Reynolds number ratios ($0.5 \leq Re^* \leq 5$) and fixed droplet parameters (Re_e, μ^*, χ, Sr) = (200, 0.2, 1.0, 0.2). (a) Time histories of lift coefficients. (b) Velocity streamlines on XOY plane at different Reynolds number ratios.

suggest that the internal Reynolds number significantly impacts droplet behaviour in shear flow, influencing the lift experienced by the droplet. However, a thorough investigation of this issue requires additional work, which would be suitable for a separate publication.

REFERENCES

- ADOUA, R., LEGENDRE, D. & MAGNAUDET, J. 2009 Reversal of the lift force on an oblate bubble in a weakly viscous linear shear flow. *J. Fluid Mech.* **628**, 23–41.
- ADOUA, S.R. 2007 Hydrodynamic of a deformed bubble in linear shear flow. *Tech. Rep.* Institut National Polytechnique.
- AOYAMA, S., HAYASHI, K., HOSOKAWA, S., LUCAS, D. & TOMIYAMA, A. 2017 Lift force acting on single bubbles in linear shear flows. *Intl J. Multiphase Flow* **96**, 113–122.
- ASMOLOV, ES2208992 1990 Dynamics of a spherical particle in a laminar boundary layer. *Fluid Dyn.* **25** (6), 886–890.
- AUTON, T.R. 1987 The lift force on a spherical body in a rotational flow. *J. Fluid Mech.* **183**, 199–218.
- AUTON, T.R., HUNT, J.C.R. & PRUD'HOMME, M. 1988 The force exerted on a body in inviscid unsteady non-uniform rotational flow. *J. Fluid Mech.* **197**, 241–257.
- BAGCHI, P. & BALACHANDAR, S. 2002 Shear versus vortex-induced lift force on a rigid sphere at moderate re . *J. Fluid Mech.* **473**, 379–388.
- BELL, J.B., COLELLA, P. & GLAZ, H.M. 1989 A second-order projection method for the incompressible Navier–Stokes equations. *J. Comput. Phys.* **85** (2), 257–283.
- BLANCO, A. & MAGNAUDET, J. 1995 The structure of the axisymmetric high-Reynolds number flow around an ellipsoidal bubble of fixed shape. *Phys. Fluids* **7** (6), 1265–1274.
- BRETHERTON, F.P. 1962 The motion of rigid particles in a shear flow at low Reynolds number. *J. Fluid Mech.* **14** (2), 284–304.
- CANDELIER, F., MEHADDI, R., MEHLIG, B. & MAGNAUDET, J. 2023 Second-order inertial forces and torques on a sphere in a viscous steady linear flow. *J. Fluid Mech.* **954**, A25.
- CHAN, P.C.-H. & LEAL, LG0402 1979 The motion of a deformable drop in a second-order fluid. *J. Fluid Mech.* **92** (1), 131–170.
- CHEN, J., HAYASHI, K., LEGENDRE, D., LUCAS, D. & TOMIYAMA, A. 2023 Effects of surfactant on lift coefficient of ellipsoidal bubbles in the viscous-force dominant regime. *Multiphase Sci. Technol.* **35** (1), 55–68.
- EDELMANN, C.A., CLERCQ, L., PATRICK, C. & NOLL, B. 2017 Numerical investigation of different modes of internal circulation in spherical drops: fluid dynamics and mass/heat transfer. *Intl J. Multiphase Flow* **95**, 54–70.
- ERVIN, E.A. & TRYGGVASON, G. 1997 The rise of bubbles in a vertical shear flow. *J. Fluids Eng.* **119** (2), 443–449.
- FANG, Z., ZHANG, J., XIONG, Q., XU, F. & NI, M. 2021 Spatiotemporal evolutions of forces and vortices of flow past ellipsoidal bubbles: direct numerical simulation based on a cartesian grid scheme. *Phys. Fluids* **33** (1), 012108.
- FENG, Z.-G. & MICHAELIDES, E.E. 2001 Drag coefficients of viscous spheres at intermediate and high Reynolds numbers. *J. Fluids Engng* **123** (4), 841–849.

- FUKUTA, M., TAKAGI, S. & MATSUMOTO, Y. 2008 Numerical study on the shear-induced lift force acting on a spherical bubble in aqueous surfactant solutions. *Phys. Fluids* **20** (4), 040704.
- HAYASHI, K., HESSENKEMPER, H., LUCAS, D., LEGENDRE, D. & TOMIYAMA, A. 2021 Scaling of lift reversal of deformed bubbles in air-water systems. *Intl J. Multiphase Flow* **142**, 103653.
- HAYASHI, K., LEGENDRE, D. & TOMIYAMA, A. 2020 Lift coefficients of clean ellipsoidal bubbles in linear shear flows. *Intl J. Multiphase Flow* **129**, 103350.
- HAYASHI, K. & TOMIYAMA, A. 2018 Effects of surfactant on lift coefficients of bubbles in linear shear flows. *Intl J. Multiphase Flow* **99**, 86–93.
- HIDMAN, N., STRÖM, H., SASIC, S. & SARDINA, G. 2022 The lift force on deformable and freely moving bubbles in linear shear flows. *J. Fluid Mech.* **952**, A34.
- HÖLZER, A. & SOMMERFELD, M. 2009 Lattice boltzmann simulations to determine drag, lift and torque acting on non-spherical particles. *Comput. Fluids* **38** (3), 572–589.
- HOMANN, H., BEC, J. & GRAUER, R. 2013 Effect of turbulent fluctuations on the drag and lift forces on a towed sphere and its boundary layer. *J. Fluid Mech.* **721**, 155–179.
- JOHNSON, T.A. & PATEL, V.C. 1999 Flow past a sphere up to a reynolds number of 300. *J. Fluid Mech.* **378**, 19–70.
- KEMPE, T., LENNARTZ, M., SCHWARZ, S. & FRÖHLICH, J. 2015 Imposing the free-slip condition with a continuous forcing immersed boundary method. *J. Comput. Phys.* **282**, 183–209.
- KIM, I. 2006 Forces on a spherical particle in shear flow at intermediate reynolds numbers. *Intl J. Comput. Fluid Dyn.* **20** (2), 137–141.
- KÜHNEL, W. 2015 *Differential Geometry*. Vol. 77. American Mathematical Society.
- KUROSE, R. & KOMORI, S. 1999 Drag and lift forces on a rotating sphere in a linear shear flow. *J. Fluid Mech.* **384**, 183–206.
- KUROSE, R., MISUMI, R. & KOMORI, S. 2001 Drag and lift forces acting on a spherical bubble in a linear shear flow. *Intl J. Multiphase Flow* **27** (7), 1247–1258.
- LEAL, L.G. 1980 Particle motions in a viscous fluid. *Annu. Rev. Fluid Mech.* **12**, 435–476.
- LEE, S. & WILCZAK, J.M. 2000 The effects of shear flow on the unsteady wakes behind a sphere at moderate reynolds numbers. *Fluid Dyn. Res.* **27** (1), 1.
- LEGENDRE, D. & MAGNAUDET, J. 1997 A note on the lift force on a spherical bubble or drop in a low-reynolds-number shear flow. *Phys. Fluids* **9** (11), 3572–3574.
- LEGENDRE, D. & MAGNAUDET, J. 1998 The lift force on a spherical bubble in a viscous linear shear flow. *J. Fluid Mech.* **368**, 81–126.
- LEGENDRE, D., RACHIH, A., SOUILLIEZ, C., CHARTON, S. & CLIMENT, É. 2019 Basset-boussinesq history force of a fluid sphere. *Phys. Rev. Fluids* **4** (7), 073603.
- LIGHTHILL, M.J. 1956 Drift. *J. Fluid Mech.* **1** (1), 31–53.
- MAGNAUDET, J. & MOUGIN, G. 2007 Wake instability of a fixed spheroidal bubble. *J. Fluid Mech.* **572**, 311–337.
- MAGNAUDET, J., TAKAGI, S.H.U. & LEGENDRE, D. 2003 Drag, deformation and lateral migration of a buoyant drop moving near a wall. *J. Fluid Mech.* **476**, 115–157.
- MCLAUGHLIN, J.B. 1991 Inertial migration of a small sphere in linear shear flows. *J. Fluid Mech.* **224**, 261–274.
- MEI, R. 1992 An approximate expression for the shear lift force on a spherical particle at finite reynolds number. *Intl J. Multiphase Flow* **18** (1), 145–147.
- MEI, R. & KLAUSNER, J.F. 1994 Shear lift force on spherical bubbles. *Intl J. Heat Fluid Flow* **15** (1), 62–65.
- NACIRI, A. 1992 Contribution à l'étude des forces exercées par un liquide sur une bulle de gaz: portance, masse ajoutée et interactions hydrodynamiques. *PhD thesis*, Ecully, Ecole centrale de Lyon.
- POPINET, S. 2003 Gerris: a tree-based adaptive solver for the incompressible Euler equations in complex geometries. *J. Comput. Phys.* **190** (2), 572–600.
- POPINET, S. 2015 A quadtree-adaptive multigrid solver for the Serre–Green–Naghdi equations. *J. Comput. Phys.* **302**, 336–358.
- RACHIH, A. 2019 Étude numérique du transfert de matière à travers l'interface d'une goutte sphérique en mouvement: mise en évidence des effets 3d. *PhD thesis*, Institut National Polytechnique de Toulouse-INPT.
- RACHIH, A., LEGENDRE, D., CLIMENT, E. & CHARTON, S. 2020 Numerical study of conjugate mass transfer from a spherical droplet at moderate Reynolds number. *Intl J. Heat Mass Trans.* **157**, 119958.
- SAFFMAN, P.G. 1965 The lift on a small sphere in a slow shear flow. *J. Fluid Mech.* **22** (2), 385–400.
- SAFFMAN, P.G. 1995 *Vortex Dynamics*. Cambridge University Press.
- SAKAMOTO, H. & HANIU, H. 1995 The formation mechanism and shedding frequency of vortices from a sphere in uniform shear flow. *J. Fluid Mech.* **287**, 151–171.

- SHI, P., CLIMENT, É. & LEGENDRE, D. 2024 Lift force on a spherical droplet in a viscous linear shear flow. *J. Fluid Mech.* **1000**, A88.
- SHI, P. & RZEHAŁ, R. 2019 Lift forces on solid spherical particles in unbounded flows. *Chem. Engng Sci.* **208**, 115145.
- SHI, P., RZEHAŁ, R., LUCAS, D. & MAGNAUDET, J. 2020 Hydrodynamic forces on a clean spherical bubble translating in a wall-bounded linear shear flow. *Phys. Rev. Fluids* **5** (7), 073601.
- SHI, P., RZEHAŁ, R., LUCAS, D. & MAGNAUDET, J. 2021 Drag and lift forces on a rigid sphere immersed in a wall-bounded linear shear flow. *Phys. Rev. Fluids* **6** (10), 104309.
- SUGIOKA, K.-I. & KOMORI, S. 2007 Drag and lift forces acting on a spherical water droplet in homogeneous linear shear air flow. *J. Fluid Mech.* **570**, 155–175.
- SUGIYAMA, K. & TAKEMURA, F. 2010 On the lateral migration of a slightly deformed bubble rising near a vertical plane wall. *J. Fluid Mech.* **662**, 209–231.
- TAKEMURA, F., TAKAGI, S.H.U., MAGNAUDET, J. & MATSUMOTO, Y. 2002 Drag and lift forces on a bubble rising near a vertical wall in a viscous liquid. *J. Fluid Mech.* **461**, 277–300.
- TAYLOR, G.I. 1932 The viscosity of a fluid containing small drops of another fluid. *Proc. R. Soc. Lond. Series A Containing Papers of a Mathematical and Physical Character* **138** (834), 41–48.
- THOMPSON, M.C., LEWEKE, T. & PROVANSAL, M. 2001 Kinematics and dynamics of sphere wake transition. *J. Fluid. Struct.* **15** (3–4), 575–585.
- TOMIYAMA, A., TAMAI, H., ZUN, I. & HOSOKAWA, S. 2002 Transverse migration of single bubbles in simple shear flows. *Chem. Engng Sci.* **57** (11), 1849–1858.
- TONG, W., YANG, Y. & WANG, S. 2021 Estimating thrust from shedding vortex surfaces in the wake of a flapping plate. *J. Fluid Mech.* **920**, A10.
- WANG, S., HE, G. & LIU, T. 2019 Estimating lift from wake velocity data in flapping flight. *J. Fluid Mech.* **868**, 501–537.
- WEI, B.-L., MENG, W.-J., NI, M.-J. & ZHANG, J. 2023 A sharp method for the simulation of flow past a liquid body with arbitrary shape and interface condition: from bubble to particle. *J. Comput. Phys.*
- WU, J.-Z., LU, X.-Y. & ZHUANG, L.-X. 2007a Integral force acting on a body due to local flow structures. *J. Fluid Mech.* **576**, 265–286.
- WU, J.-Z., MA, H.-Y. & ZHOU, M.-D. 2007b *Vorticity and Vortex Dynamics*. Springer Science & Business Media.
- WU, J.-Z., PAN, Z.-L. & LU, X.-Y. 2005 Unsteady fluid-dynamic force solely in terms of control-surface integral. *Phys. Fluids* **17** (9), 098102.
- ZENIT, R. & MAGNAUDET, J. 2009 Measurements of the streamwise vorticity in the wake of an oscillating bubble. *Intl J. Multiphase Flow* **35** (2), 195–203.
- ZHANG, J. & NI, M.-J. 2017 What happens to the vortex structures when the rising bubble transits from zigzag to spiral? *J. Fluid Mech.* **828**, 353–373.
- ZHANG, J., NI, M.-J. & MAGNAUDET, J. 2021 Three-dimensional dynamics of a pair of deformable bubbles rising initially in line. part 1. moderately inertial regimes. *J. Fluid Mech.* **920**, A16.